


Article

GF-2 Data for Lithological Classification Using Texture Features and PCA/ICA Methods in Jixi, Heilongjiang, China

Tianyi Chen , Changbao Yang *, Ligu Han and Senmiao Guo

College of Geo-Exploration Science and Technology, Jilin University, Changchun 130026, China

* Correspondence: yangcb@jlu.edu.cn; Tel.: +86-133-3169-7295

Abstract: Lithological classification is a pivotal aspect in the field of geology, and traditional field surveys are inefficient and challenging in certain areas. Remote sensing technology offers advantages such as high efficiency and wide coverage, providing a solution to the aforementioned issues. The aim of this study is to apply remote sensing technology for lithological classification and attempt to enhance the accuracy of classification. Taking a study area in Jixi, Heilongjiang Province, China, as an example, lithological classification is conducted using high-resolution satellite remote sensing data from GF-2 and texture data based on gray-level co-occurrence matrix (GLCM). By comparing the accuracy of lithological classification using different methods, the support vector machine (SVM) method with the highest overall accuracy is selected for further investigation. Subsequently, this study compares the effects of combining GF-2 data with different texture data, and the results indicate that combining textures can effectively improve the accuracy of lithological classification. In particular, the combination of GF-2 and the Dissimilarity index performs the best among single-texture combinations, with an overall accuracy improvement of 7.8630% (increasing from 74.6681% to 82.5311%) compared to using only GF-2 data. In the multi-texture combination dataset, the Mean index is crucial for enhancing classification accuracy. Selecting appropriate textures for combination can effectively improve classification accuracy, but it is important to note that excessive overlaying of textures may lead to a decrease in accuracy. Furthermore, this study employs principal component analysis (PCA) and independent component analysis (ICA) to process the GF-2 data and combines the resulting PCA and ICA datasets with different texture data for lithological classification. The results demonstrate that combining PCA and ICA with texture data further enhances classification accuracy. In conclusion, this study demonstrates the application of remote sensing technology in lithological classification, with a focus on exploring the application value of different combinations of multispectral data, texture data, PCA data, and ICA data. These findings provide valuable insights for future research in this field.

Keywords: GF-2; lithological classification; GLCM; SVM; ICA; PCA

Citation: Chen, T.; Yang, C.; Han, L.; Guo, S. GF-2 Data for Lithological Classification Using Texture Features and PCA/ICA Methods in Jixi, Heilongjiang, China. *Remote Sens.* **2023**, *15*, 4676. <https://doi.org/10.3390/rs15194676>

Academic Editors: Kevin Tansey and Robert Hewson

Received: 6 July 2023

Revised: 18 September 2023

Accepted: 21 September 2023

Published: 24 September 2023



Copyright: © 2023 by the authors. Licensee MDPI, Basel, Switzerland. This article is an open access article distributed under the terms and conditions of the Creative Commons Attribution (CC BY) license (<https://creativecommons.org/licenses/by/4.0/>).

1. Introduction

Geological research holds undeniable significance for human society, with close ties to socioeconomic development and numerous benefits for various aspects of human production and life. Geological maps, serving as vital instruments for communicating geological research findings, have witnessed continuous advancement and refinement since the early 19th century, when British geologist William Smith laid the groundwork for modern geological mapping.

A key aspect of geological mapping is the identification and classification of lithology. Although traditional field investigation and mapping are relatively accurate, they are inefficient and difficult to implement in certain areas [1–3]. Remote sensing technology possesses advantages, such as high efficiency, cost-effectiveness, and wide coverage, providing a solution to the aforementioned issues [4–14]. By utilizing remote sensing technology, a broad range of surface information can be obtained, enabling large-scale lithological

classification and providing fundamental data for geological research. Remote sensing lithological classification can also guide mineral resource exploration, improving efficiency and accuracy in exploration efforts. Additionally, remote sensing lithological classification can facilitate the prediction and assessment of potential geological hazards, allowing for the timely implementation of corresponding disaster prevention and mitigation measures, thereby reducing the impact of geological disasters on human activities and the ecological environment. Furthermore, remote sensing lithological classification can be employed in environmental monitoring, such as detecting rock dissolution pollution in water bodies and mapping wetland vegetation distribution, among others. In conclusion, the use of remote sensing technology for lithological classification holds significant practical importance in geological research, resource exploration, disaster prediction and prevention, and environmental monitoring [15–21].

Theoretically, each type of rock has its own unique spectral characteristics, but in practical remote sensing applications, these spectra are affected by many factors, such as atmospheric effects, coverage of soil and vegetation, and resolution of multispectral data [22]. These factors can limit the accuracy of lithological classification.

Some studies have found that combining texture information can enhance classification accuracy [23,24]. Texture, as an important spatial feature of images, has been widely used in various image processing fields [25,26]. However, texture does not have a precise mathematical definition [27], which is also why there are various texture analysis methods [28]. Although there are many studies on image texture, few have focused on the effect of different combinations of texture information from remote sensing data on improving lithological mapping accuracy.

The GF-2 satellite is China's first civil optical remote sensing satellite with a spatial resolution of over 1 m [29]. Since its launch in August 2014, GF-2 has continuously provided remote sensing data for relevant work. Regrettably, the potential of GF-2 data in the field of lithological classification has remained largely unexplored.

This passage aims to explore the contribution of different texture features to lithological classification by comparing their effects. By utilizing various combinations of texture features and evaluating their impact on lithological classification, this study may provide methods and criteria for feature selection and combination in future research. The GF-2 data were processed using principal component analysis (PCA) and independent component analysis (ICA) techniques, in conjunction with texture features, to explore the potential value of these method combinations in lithological classification. This will assist in guiding the selection of data processing techniques in similar future studies and provide additional options for lithological classification.

This study uses GF-2 satellite data to conduct lithological classification research in Jixi City, Heilongjiang Province, China. The objectives of this study are: (1) to compare the classification accuracy of four methods, including minimum distance classification, maximum likelihood classification, neural network classification, and support vector machine classification, and select the method with the highest accuracy for lithological classification using GF-2 data; (2) to use GF-2 data combined with different texture features for lithological classification and compare the effects of different texture features on lithological classification; (3) to use multiple-texture features for different combinations and evaluate the effects of different combination methods on lithological classification; (4) to process GF-2 data using PCA and ICA methods and combine them with texture features for lithological classification. The effectiveness of PCA and ICA in lithological classification and the impact of different data combinations on lithological classification will be evaluated.

2. Materials and Methods

2.1. Description of Study Area

The study area was located in Jixi City, southeastern Heilongjiang Province, China, as shown in Figure 1. Jixi City is connected to Shuangyashan City and Qitaihe City in the north, Russia in the east and south, and Mudanjiang City in the southwest. The

geomorphology of Jixi City primarily consists of the Songnen Plain, hills, low mountains, and some mountainous areas. The Songnen Plain is the dominant landform in the region, with relatively flat terrain. The area belongs to the temperate zone, with a monsoon climate characterized by short and warm summers and long and cold winters. Precipitation is concentrated in the summer, and the average annual rainfall is abundant. The vegetation types in the area mainly include coniferous forests, broad-leaved forests, grasslands, and wetlands [30]. The northwestern, northern, and northeastern regions of the study area are primarily characterized by sediments, including gravel, sand, silt, and clay. In the remaining areas, igneous rocks, such as Syenogranite and Granodiorite, predominate.

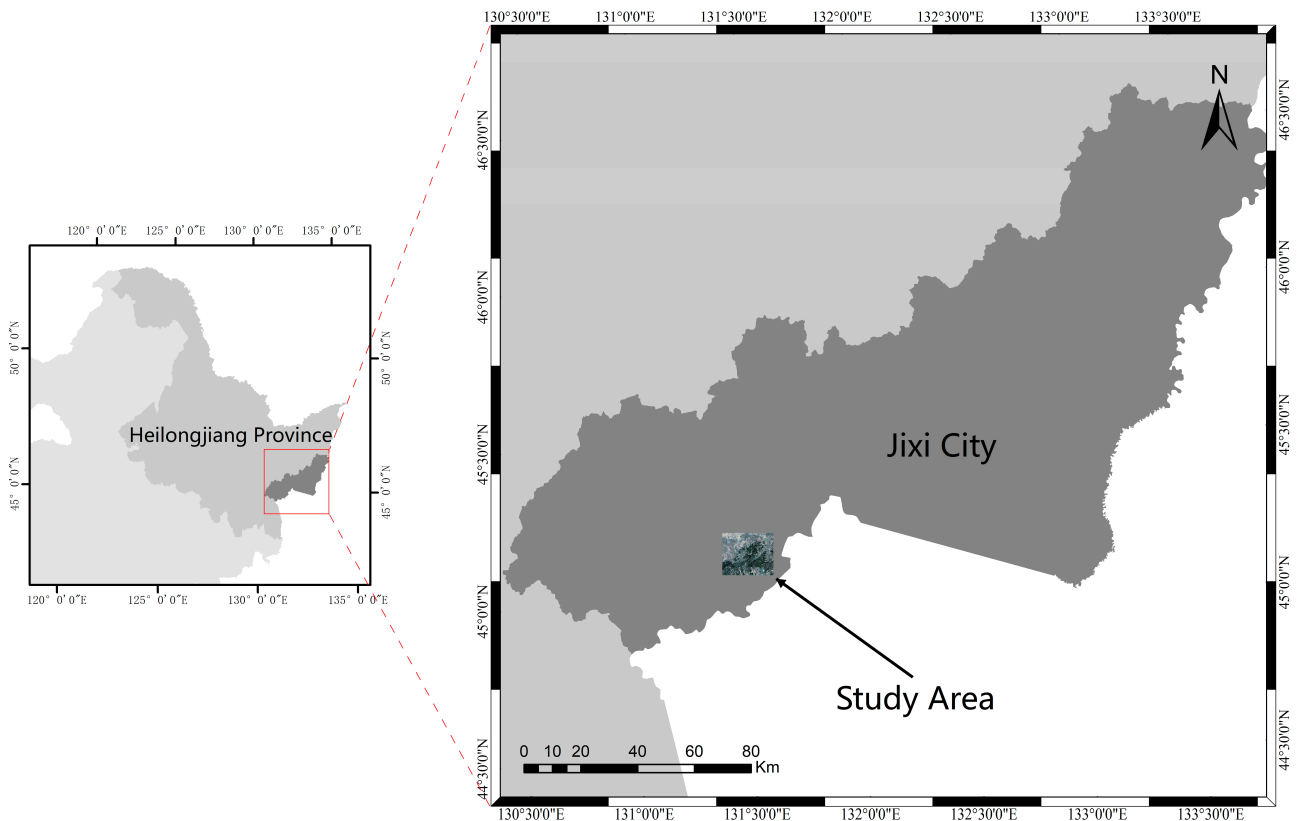


Figure 1. Location map. The study area is located in Jixi City, Heilongjiang Province, China.

The geological map shown in Figure 2 was generated through multiple steps. Firstly, field investigations were conducted in the study area to collect preliminary geological information. Secondly, the obtained field data were integrated and supplemented with existing geological maps and remote sensing data. Lastly, the integrated data were digitized and processed using a geographic information system (GIS) to generate the geological map with a scale of 1:250,000. The samples used in this study were derived from the results of the field investigations.

2.2. Data and Data Preprocessing

GF-2 image data consist of one panchromatic band and four multispectral bands [31], with spectral characteristics shown in Table 1. The GF-2 image data used in this study were acquired on 25 October 2020 and projected using the Universal Transverse Mercator (WGS 1984 datum, Zone 52N). The multispectral images were radiometrically calibrated, followed by atmospheric correction and orthorectification. The panchromatic image was also radiometrically calibrated and orthorectified. The nearest neighbor diffusion (NNDiffuse) pan sharpening algorithm was used to fuse the calibrated multispectral images with the panchromatic image, which was recently proposed by the Rochester Institute of Technology (RIT) with a suitable image fusion effect [29]. The fused images were then resampled to a

15 m resolution and cropped to obtain a study area of 1000 rows and 1200 columns. All these preprocessing steps were performed in ENVI 5.3 software. Figure 3 shows the flow chart of the lithological classification process.

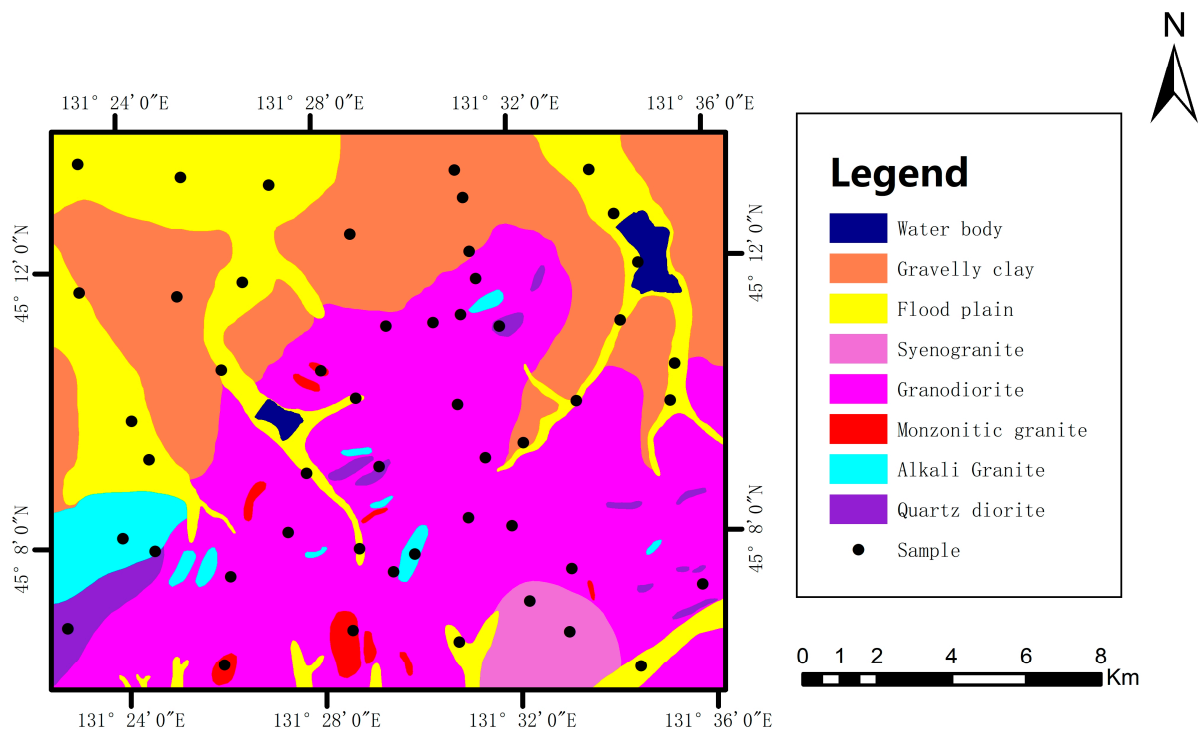


Figure 2. Geological map of the study area.

Table 1. Spectral characteristics of GaoFen-2 (GF-2) data.

Bands	Spectral Range (nm)	Spatial Resolution (m)
Pan	450–900	0.8
Blue	450–520	
Green	520–590	3.2
Red	630–690	
NIR	770–890	

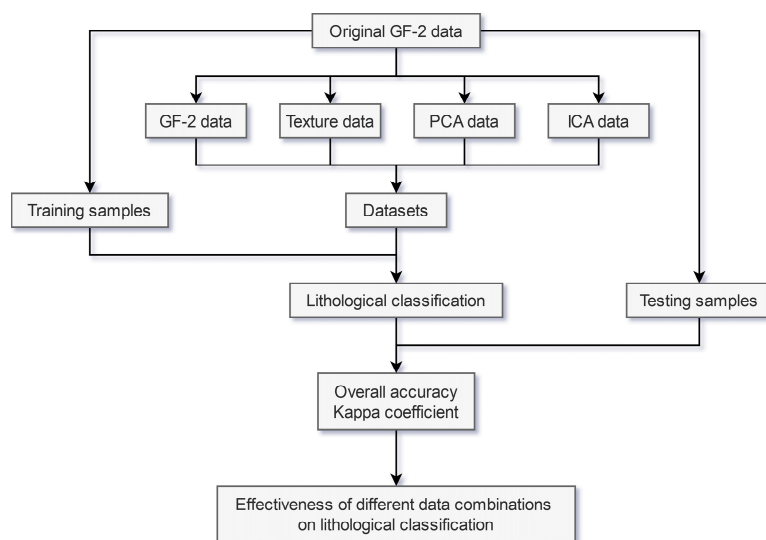


Figure 3. Flow chart of the lithological classification process.

2.3. Training and Testing Samples

The careful selection of training and testing samples was conducted utilizing the geological map shown in Figure 2 and field survey samples, in combination with visual interpretation. A total of 10 classes were chosen, as presented in Table 2. To minimize the possibility of overfitting, the training samples for each class were ensured to be at least several times the number of data layers to be used for classification.

Table 2. The training and testing samples.

Class Name	Training Sample (Pixels)	Testing Sample (Pixels)
Vegetation	325	344
Water body	1888	1185
Buildings	1269	1583
Gravelly clay	1710	1460
Flood plain	3310	3066
Syenogranite	552	506
Granodiorite	4827	4520
Monzonitic granite	579	507
Alkali granite	1200	869
Quartz diorite	896	649

2.4. Lithological Classification Methods

Four methods were used for lithological classification in this study, including minimum distance classification, maximum likelihood classification, neural network classification, and support vector machine classification. All these four methods were implemented in ENVI 5.3 software, and a brief introduction to these four algorithms is provided below.

2.4.1. Minimum Distance Classification

Minimum distance classification is the most basic classification method and assigns an unknown pixel to the class with the smallest Euclidean distance to it [6,32].

2.4.2. Maximum Likelihood Classification

Maximum likelihood classification is one of the most commonly used supervised classification methods in remote sensing. It uses statistical analysis to calculate probability density functions and assigns an unknown pixel to the class with the highest probability [33,34].

2.4.3. Neural Network Classification

Neural network classification is one of the mainstream machine learning methods and establishes a model by simulating the way the human neural system recognizes and learns [35]. This neural network model consists of many nodes, which are connected by weighted connections and adjust the weights continuously during the training process until the best output is obtained.

2.4.4. Support Vector Machine Classification

Support vector machine classification is one of the most widely used machine learning methods. It maximizes the margin between classes by seeking an optimal separating hyperplane [36,37]. Soft margin techniques and penalty parameters are introduced to improve the generalization ability when the data contain outliers and classes are not linearly separable [22].

2.5. Texture Analysis Methods

Texture is an important feature for identifying image classes [38,39], and there are many methods for defining texture. Among them, the gray-level co-occurrence matrix (GLCM) has been proven to be effective in rock texture analysis [40]. The principle of GLCM is to quantize the gray levels of the original grayscale matrix, establish a GLCM

based on the frequency of specific pixel pairs, and calculate different indicators based on the GLCM [41–43]. This paper uses 8 different GLCM indicators, which are briefly introduced below (where $g(i, j)$ is the normalized value of the frequency of pixel pair (i, j) and μ and σ^2 are the mean and variance of the GLCM, respectively).

2.5.1. Contrast

The Contrast index is used to measure the drastic changes in image grayscale. The clearer and finer the texture of an image, the higher the Contrast value.

The Contrast index provides information about the brightness contrast in rock textures. The Contrast index is of significant importance in describing the details, edges, and variability of rock textures.

The Contrast index measures the degree of difference between adjacent gray-level pixels in rock textures. It helps us understand the contrast and texture variation between gray-level pixels in rock textures. A higher Contrast value indicates a greater difference between adjacent gray-level pixels and a more noticeable texture variation in the rock texture. Conversely, a lower Contrast value indicates relatively similar adjacent gray-level pixels and a smaller texture variation in the rock texture.

In rock texture analysis, the Contrast index can be used to assess the texture variation and edge features of rock textures. Different types of rocks or textures often exhibit different texture features, which are reflected in different Contrast values in terms of the contrast and texture variation between gray-level pixels. Rock textures with complex texture variations and rich edges tend to have higher Contrast values, while relatively uniform and smooth rock textures exhibit lower Contrast values.

The corresponding Contrast data are obtained through calculations using GF-2 data. In subsequent research, the Contrast data will be combined with other data to explore the contribution of this texture index to lithological classification.

$$Contrast = \sum_i \sum_j (i - j)^2 \cdot g(i, j) \quad (1)$$

2.5.2. Correlation

The Correlation index is used to measure the linear correlation of image grayscale. The higher the linear correlation between the grayscale levels of adjacent pixels in an image, the larger the Correlation value.

The Correlation index provides information about the correlation of grayscale values between pixels in rock textures. The Correlation index is highly useful for describing the linearity, directionality, and regularity of rock textures.

The Correlation index measures the linear correlation of pixel values in rock textures. It helps us understand the linear relationship between different grayscale-level pixels in rock textures. A Correlation value closer to 1 indicates a strong linear correlation between pixel values in the rock texture, suggesting a tendency toward a regular and orderly texture. Conversely, a Correlation value closer to 0 indicates less correlation between pixel values in the rock texture, suggesting a tendency toward randomness and disorder in the texture.

In rock texture analysis, the Correlation index can be used to assess the directionality of rock textures. Different types of rocks often exhibit different degrees of linearity and regularity, which are reflected in different correlation characteristics of their texture features. A higher Correlation value implies the presence of significant directional features in the rock texture, while a lower Correlation value indicates a weaker directionality. Directionality is an important distinguishing factor for certain types of rocks.

The corresponding Correlation data are obtained through calculations using GF-2 data. In subsequent research, the Correlation data will be combined with other data to explore the contribution of this texture index to lithological classification.

$$Correlation = \sum_i \sum_j \frac{(i - \mu) \cdot (j - \mu) \cdot g(i, j)}{\sigma^2} \quad (2)$$

2.5.3. Dissimilarity

The Dissimilarity index is used to measure the changes in image grayscale, similar to Contrast, but with a difference in that exponential weighting is used in Contrast, whereas linear weighting is used in Dissimilarity.

The Dissimilarity index provides information about the degree of difference between pixels of different grayscale levels in rock textures. The Dissimilarity index is highly useful for describing the level of variation, roughness, and granularity of rock textures.

The Dissimilarity index measures the degree of difference between pixels of different grayscale levels in rock textures. It helps us understand the level of variation between pixels of different grayscale levels in rock textures, i.e., the differences in pixel values. A higher Dissimilarity value indicates a greater difference between different regions in the rock texture, suggesting a tendency toward roughness and granularity. Conversely, a lower Dissimilarity value indicates less difference between different regions in the rock texture, suggesting a tendency toward uniformity and smoothness.

In rock texture analysis, the Dissimilarity index can be used to identify different types of rock textures. Different rock types often exhibit different levels of variation and granularity, which are reflected in different characteristics of their texture features. Rough rock textures tend to have higher Dissimilarity values, indicating larger differences in pixel values within the texture. On the other hand, smooth rock textures exhibit lower Dissimilarity values, indicating relatively smaller differences in pixel values within the texture.

The corresponding Dissimilarity data are obtained through calculations using GF-2 data. In subsequent research, the Dissimilarity data will be combined with other data to explore the contribution of this texture index to lithological classification.

$$Dissimilarity = \sum_i \sum_j |i - j| \cdot g(i, j) \quad (3)$$

2.5.4. Entropy

The Entropy index is used to measure the disorderliness of image grayscale. The more disorderly and complex the grayscale distribution of an image, the higher the Entropy value. When the values in the GLCM are uniformly distributed, the Entropy value is higher.

The Entropy index provides information about the complexity, uncertainty, and information content in rock textures. The Entropy index is highly useful for describing the texture richness, variation, and level of detail in rock textures.

The Entropy index measures the degree of chaos in the distribution of grayscale levels in rock textures. It helps us understand the uncertainty and complexity of the texture in rock textures. A higher Entropy value indicates a more uniform and complex distribution of grayscale levels in the rock texture, suggesting a tendency toward richness and variation in the texture. Conversely, a lower Entropy value indicates a more concentrated distribution of grayscale levels in the rock texture, suggesting a tendency toward simplicity and uniformity.

In rock texture analysis, the Entropy index can be used to evaluate the level of detail in rock textures. Different rock types often exhibit different levels of complexity and texture richness, which are reflected in different degrees of uncertainty in the distribution of grayscale levels. Rock textures with abundant details tend to have higher Entropy values, indicating a more complex distribution of grayscale levels. On the other hand, rocks with simpler textures exhibit lower Entropy values, indicating a relatively concentrated distribution of grayscale levels.

The corresponding Entropy data are obtained through calculations using GF-2 data. In subsequent research, the Entropy data will be combined with other data to explore the contribution of this texture index to lithological classification.

$$Entropy = -\sum_i \sum_j \log(g(i, j)) \cdot g(i, j) \quad (4)$$

2.5.5. Homogeneity

The Homogeneity index, also known as the inverse difference moment, is used to measure the homogeneity of an image. When the grayscale of an image is uniform, Homogeneity value is at its maximum.

The Homogeneity index provides information about the similarity and consistency between pixels of different grayscale levels in rock textures. The Homogeneity index is highly useful for describing the uniformity, smoothness, and proximity between pixels in rock textures.

The Homogeneity index measures the degree of proximity between pixels of different grayscale levels in rock textures. It helps us understand the similarity and consistency between adjacent grayscale-level pixels in rock textures. A higher Homogeneity value indicates smaller differences in grayscale between adjacent pixels in the rock texture, suggesting a tendency toward uniformity and smoothness in the texture. Conversely, a lower Homogeneity value indicates larger differences in grayscale between adjacent pixels in the rock texture, suggesting a tendency toward non-uniformity and roughness in the texture.

In rock texture analysis, the Homogeneity index can be used to evaluate the roughness and granularity of rock textures. Different rock types often exhibit different levels of uniformity and smoothness, which are reflected in different characteristics of grayscale differences between adjacent pixels. Rough rock textures tend to have lower Homogeneity values, indicating larger differences in grayscale between adjacent pixels. On the other hand, smooth rock textures exhibit higher Homogeneity values, indicating relatively smaller differences in grayscale between adjacent pixels.

The corresponding Homogeneity data are obtained through calculations using GF-2 data. In subsequent research, the Homogeneity data will be combined with other data to explore the contribution of this texture index to lithological classification.

$$\text{Homogeneity} = \sum_i \sum_j \frac{g(i, j)}{1 + (i - j)^2} \quad (5)$$

2.5.6. Mean

The Mean index is used to measure the average grayscale of an image.

The Mean index provides information about the average grayscale value in rock textures. The Mean index is highly useful for describing the brightness and grayscale distribution in rock textures.

The Mean index measures the average value of grayscale levels in rock textures. It helps us understand the overall brightness of grayscale levels in rock textures. The Mean value reflects the central position of the pixel grayscale distribution in the rock texture. A higher Mean value indicates a higher overall brightness, while a lower Mean value indicates a lower overall brightness.

In rock texture analysis, the Mean index can be used to evaluate the brightness level of rock textures. Different rock types often exhibit different brightness and grayscale distribution characteristics. Rock textures with higher brightness tend to have higher Mean values, while rock textures with lower brightness exhibit lower Mean values.

Furthermore, it is important to note that the Mean index can only provide overall brightness information about grayscale levels in rock textures and cannot provide detailed information about the distribution range or shape of grayscale levels. Therefore, in rock texture analysis, it is common to combine other GLCM indices or image processing methods for comprehensive analysis.

The corresponding Mean data are obtained through calculations using GF-2 data. In subsequent research, the Mean data will be combined with other data to explore the contribution of this texture index to lithological classification.

$$\text{Mean} = \sum_i \sum_j i \cdot g(i, j) \quad (6)$$

2.5.7. Second Moment

The Second Moment index is used to measure the regularity of grayscale distribution in an image. Second Moment is negatively correlated with Entropy, and the more uniform and regular the texture of an image, the higher the value of Second Moment. When the values of GLCM are uniformly distributed, the Second Moment value is lower.

The Second Moment index provides information about the uniformity of grayscale-level pixel distribution and texture details in rock textures. The Second Moment index is highly useful for describing the uniformity, level of detail, and smoothness of rock textures.

The Second Moment index measures the uniformity of grayscale-level pixel distribution or the smoothness of texture in rock textures. It helps us understand the overall distribution characteristics of grayscale-level pixels in rock textures. A higher Second Moment value indicates a more uniform distribution of grayscale-level pixels in the rock texture, indicating a tendency toward smoothness in the texture. Conversely, a lower Second Moment value suggests an uneven distribution of grayscale-level pixels in the rock texture, indicating a tendency toward roughness and potentially more texture details and variations.

In rock texture analysis, the Second Moment index can be used to evaluate the level of detail and variability in rock textures. Different rock types or texture types often exhibit different texture characteristics, which are reflected in the energy or Second Moment values of grayscale-level distributions and texture details. Rock textures with rich details and high variability tend to have lower Second Moment values, while relatively uniform and smooth rock textures exhibit higher Second Moment values.

The corresponding Second Moment data are obtained through calculations using GF-2 data. In subsequent research, the Second Moment data will be combined with other data to explore the contribution of this texture index to lithological classification.

$$\text{Second Moment} = \sum_i \sum_j g^2(i, j) \quad (7)$$

2.5.8. Variance

The Variance index is used to measure the variance of image grayscale. The higher the discreteness of grayscale distribution, the larger the Variance value.

The Variance index provides information about the variability and texture roughness of grayscale-level pixels in rock textures. The Variance index is highly useful for describing the differences, roughness, and dispersion of grayscale-level pixels in rock textures.

The Variance index measures the differences and dispersion of grayscale-level pixels in rock textures. It helps us understand the variability of grayscale-level pixels and the roughness of the texture in rock textures. A higher Variance value indicates greater differences and dispersion of grayscale-level pixels in the rock texture, indicating a rougher texture. Conversely, a lower Variance value suggests a relatively uniform and dense distribution of grayscale-level pixels in the rock texture, indicating smoother texture.

In rock texture analysis, the Variance index can be used to evaluate the roughness and variability of rock textures. Different rock types or texture types often exhibit different detail characteristics, which are reflected in the differences and dispersion of grayscale-level pixels and the resulting Variance values. Rock textures with rougher surfaces and higher variability tend to have higher Variance values, while relatively smooth and consistent rock textures exhibit lower Variance values.

Furthermore, it is important to note that the Variance index can only provide information about the dispersion of grayscale-level pixels in rock textures and cannot provide specific details about grayscale-level distributions and texture morphology. Therefore, in rock texture analysis, it is common to combine other GLCM indices or image processing methods for comprehensive analysis.

The corresponding Variance data are obtained through calculations using GF-2 data. In subsequent research, the Variance data will be combined with other data to explore the contribution of this texture index to lithological classification.

$$\text{Variance} = \sum_i \sum_j (i - \mu)^2 \cdot g(i, j) \quad (8)$$

2.6. Image Processing Methods

This paper employs two image enhancement processing algorithms, namely principal component analysis (PCA) and independent component analysis (ICA). The following provides a brief introduction to these two methods.

2.6.1. Principal Component Analysis

The core idea of PCA is to reduce the complexity of high-dimensional data while preserving the original trends and patterns as much as possible [44,45]. PCA projects the data onto a new principal component space by a linear transformation. From a geometric point of view, the coordinate system of the transformed principal component space rotates at an angle compared to the original coordinate system. The direction of the new axes points toward the direction with large amounts of data information. These axis directions are the principal component directions, which are mutually independent and maintain the same sum of variances before and after transformation. Research shows that PCA has great potential in identifying lithology in multispectral remote sensing images [4,46–48].

2.6.2. Independent Component Analysis

Similar to PCA, ICA projects the data onto a new space. However, ICA is based on the non-Gaussian assumption of independent sources. The projected axes are directed toward independent directions, and these independent components provide an approximate estimation of source signals [49]. Statistically speaking, the concept of statistical independence adopted by ICA is stronger than that of uncorrelatedness. Essentially, if two variables are independent, then any value of one variable cannot provide any information about the value of the other variable. If two variables are uncorrelated, however, the value of one variable can provide information about the value of the other variable [50]. Evidence suggests that ICA performs well in feature extraction of remote sensing data [51–54].

2.7. Data Combination

Eight different texture indices were employed for lithological classification, and different combinations of data were evaluated, as shown in Table 3. Firstly, the GF-2 data were combined with each of the eight different texture indices separately to classify lithology and evaluate the role of different texture indices in lithological classification. Secondly, the eight different texture indices were combined in pairs to obtain 28 different combinations of data. The GF-2 data were combined with these 28 different datasets respectively to classify lithology, and the effects of different combinations were evaluated to identify the better-performing texture indices. Thirdly, various further combinations of data were evaluated based on the results of the first two experiments to assess the effect of different combination methods on lithological classification.

Table 3. Datasets for lithological classification.

Dataset	Abbreviation	Number of Data Layers
GF-2 + Contrast	GF2_Con	8
GF-2 + Correlation	GF2_Corr	8
GF-2 + Dissimilarity	GF2_D	8
GF-2 + Entropy	GF2_E	8
GF-2 + Homogeneity	GF2_H	8

Table 3. Cont.

Dataset	Abbreviation	Number of Data Layers
GF-2 + Mean	GF2_M	8
GF-2 + Second Moment	GF2_S	8
GF-2 + Variance	GF2_V	8
GF-2 + Contrast + Correlation	GF2_Con_Corr	12
GF-2 + Contrast + Dissimilarity	GF2_Con_D	12
GF-2 + Contrast + Entropy	GF2_Con_E	12
GF-2 + Contrast + Homogeneity	GF2_Con_H	12
GF-2 + Contrast + Mean	GF2_Con_M	12
GF-2 + Contrast + Second Moment	GF2_Con_S	12
GF-2 + Contrast + Variance	GF2_Con_V	12
GF-2 + Correlation + Dissimilarity	GF2_Corr_D	12
GF-2 + Correlation + Entropy	GF2_Corr_E	12
GF-2 + Correlation + Homogeneity	GF2_Corr_H	12
GF-2 + Correlation + Mean	GF2_Corr_M	12
GF-2 + Correlation + Second Moment	GF2_Corr_S	12
GF-2 + Correlation + Variance	GF2_Corr_V	12
GF-2 + Dissimilarity + Entropy	GF2_D_E	12
GF-2 + Dissimilarity + Homogeneity	GF2_D_H	12
GF-2 + Dissimilarity + Mean	GF2_D_M	12
GF-2 + Dissimilarity + Second Moment	GF2_D_S	12
GF-2 + Dissimilarity + Variance	GF2_D_V	12
GF-2 + Entropy + Homogeneity	GF2_E_H	12
GF-2 + Entropy + Mean	GF2_E_M	12
GF-2 + Entropy + Second Moment	GF2_E_S	12
GF-2 + Entropy + Variance	GF2_E_V	12
GF-2 + Homogeneity + Mean	GF2_H_M	12
GF-2 + Homogeneity + Second Moment	GF2_H_S	12
GF-2 + Homogeneity + Variance	GF2_H_V	12
GF-2 + Mean + Second Moment	GF2_M_S	12
GF-2 + Mean + Variance	GF2_M_V	12
GF-2 + Second Moment + Variance	GF2_S_V	12
GF-2 + Correlation + Dissimilarity + Entropy	GF2_Corr_D_E	16
GF-2 + Correlation + Dissimilarity + Mean	GF2_Corr_D_M	16
GF-2 + Correlation + Dissimilarity + Second Moment	GF2_Corr_D_S	16
GF-2 + Correlation + Entropy + Mean	GF2_Corr_E_M	16
GF-2 + Correlation + Entropy + Second Moment	GF2_Corr_E_S	16
GF-2 + Correlation + Mean + Second Moment	GF2_Corr_M_S	16
GF-2 + Dissimilarity + Entropy + Mean	GF2_D_E_M	16
GF-2 + Dissimilarity + Entropy + Second Moment	GF2_D_E_S	16
GF-2 + Dissimilarity + Mean + Second Moment	GF2_D_M_S	16
GF-2 + Entropy + Mean + Second Moment	GF2_E_M_S	16
GF-2 + Correlation + Dissimilarity + Entropy + Mean	GF2_Corr_D_E_M	20
GF-2 + Correlation + Dissimilarity + Entropy + Second Moment	GF2_Corr_D_E_S	20
GF-2 + Correlation + Dissimilarity + Mean + Second Moment	GF2_Corr_D_M_S	20
GF-2 + Correlation + Entropy + Mean + Second Moment	GF2_Corr_E_M_S	20
GF-2 + Dissimilarity + Entropy + Mean + Second Moment	GF2_D_E_M_S	20
GF-2 + Correlation + Dissimilarity + Entropy + Mean + Second Moment	GF2_Corr_D_E_M_S	24

Table 3. Cont.

Dataset	Abbreviation	Number of Data Layers
GF-2 + Contrast + Correlation + Dissimilarity + Entropy + Mean + Second Moment	GF2_Con_Corr_D_E_M_S	28
GF-2 + Correlation + Dissimilarity + Entropy + Homogeneity + Mean + Second Moment	GF2_Corr_D_E_H_M_S	28
GF-2 + Correlation + Dissimilarity + Entropy + Mean + Second Moment + Variance	GF2_Corr_D_E_M_S_V	28
GF-2 + Contrast + Correlation + Dissimilarity + Entropy + Homogeneity + Mean + Second Moment	GF2_Con_Corr_D_E_H_M_S	32
GF-2 + Contrast + Correlation + Dissimilarity + Entropy + Mean + Second Moment + Variance	GF2_Con_Corr_D_E_M_S_V	32
GF-2 + Correlation + Dissimilarity + Entropy + Homogeneity + Mean + Second Moment + Variance	GF2_Corr_D_E_H_M_S_V	32
GF-2 + Contrast + Correlation + Dissimilarity + Entropy + Homogeneity + Mean + Second Moment + Variance	GF2_Con_Corr_D_E_H_M_S_V	36

3. Results

This section evaluated the performance of lithological classification using a confusion matrix, with measures such as overall accuracy, Kappa coefficient, producer's accuracy, and user's accuracy. Overall accuracy is obtained by dividing the number of correctly classified pixels by the total number of pixels. The Kappa coefficient is a measure of consistency that accounts well for small samples. The producer's accuracy is the probability of correctly classifying pixels with the true class X, while the user's accuracy is the probability of pixels classified as X being truly of class X.

3.1. Lithological Classification Based on Different Methods

Figure 4 shows the results of lithological classification on GF-2 data using four different methods: minimum distance classification, maximum likelihood classification, neural network classification, and support vector machine classification. Table 4 presents the overall accuracy and Kappa coefficient obtained using these methods. Results show that the overall accuracy and Kappa coefficient obtained using the minimum distance classification method are the lowest. From the comparison of the four figures, it can be observed that this method poorly separates Buildings, and there are many misclassifications for Gravelly clay and Flood plain, resulting in significant noise. The overall accuracy and Kappa coefficient obtained using the maximum likelihood classification method are better than those obtained using the minimum distance classification. Compared to the minimum distance classification, the maximum likelihood classification significantly improves the classification of Buildings, with many misclassifications corrected and some noise eliminated. However, the maximum likelihood classification method still exhibits noticeable problems of misclassification with Granodiorite and over-classification with Alkali granite. The overall accuracy and Kappa coefficient of neural network classification and support vector machine classification methods are similar and higher than those of the maximum likelihood classification method, indicating their superior classification performance. Due to its slightly higher overall accuracy, we adopted the support vector machine classification method for subsequent studies.

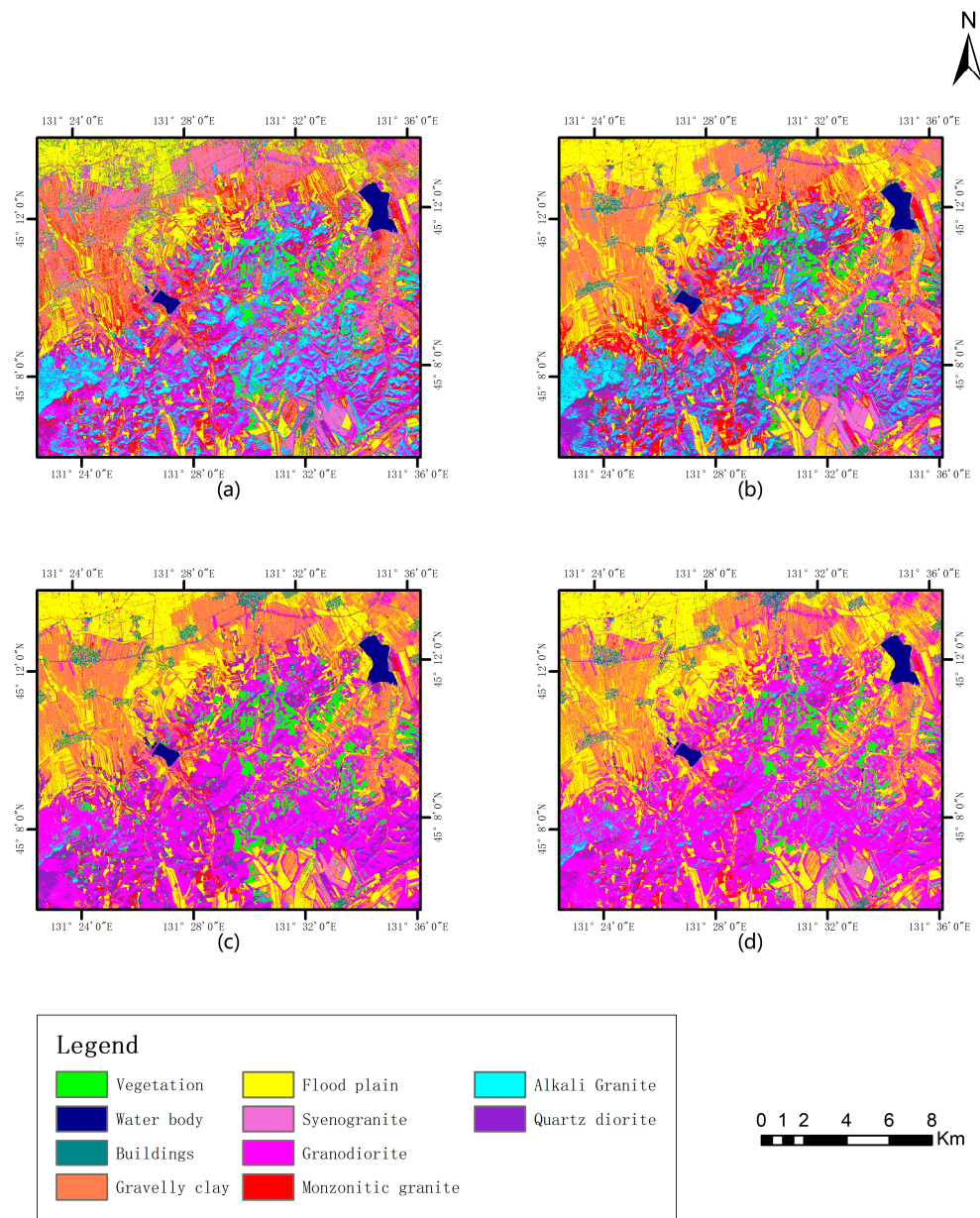


Figure 4. The lithological classification of the GF-2 dataset using different methods. (a) Minimum distance classification; (b) maximum likelihood classification; (c) neural network classification; (d) support vector machine classification.

Table 4. The lithological classification accuracies of the GF-2 dataset using different methods.

Classification Method	Overall Accuracy (%)	Kappa Coefficient
Minimum distance classification	57.3218	0.5075
Maximum likelihood classification	68.8066	0.6418
Neural network classification	73.2317	0.6750
Support vector machine classification	74.6681	0.6869

3.2. Lithological Classification Based on Different Texture Features

Figure 5 shows the results of lithological classification using the support vector machine classification method on nine different datasets. Table 5 presents the overall accuracy and Kappa coefficient obtained from these nine datasets for comparison. The results indicate that the incorporation of texture features generally improves the classification accuracy

compared to using the GF-2 data alone, suggesting the effectiveness of texture features in lithological classification. Among the nine datasets, GF2_D has the highest overall accuracy at 82.5311%, followed by GF2_E (81.5712%), GF2_S (81.3125%), and GF2_M (81.1151%), which all exhibit significant improvements in classification accuracy. GF2_Corr has the lowest overall accuracy of 77.1257% among the eight datasets, including texture features.

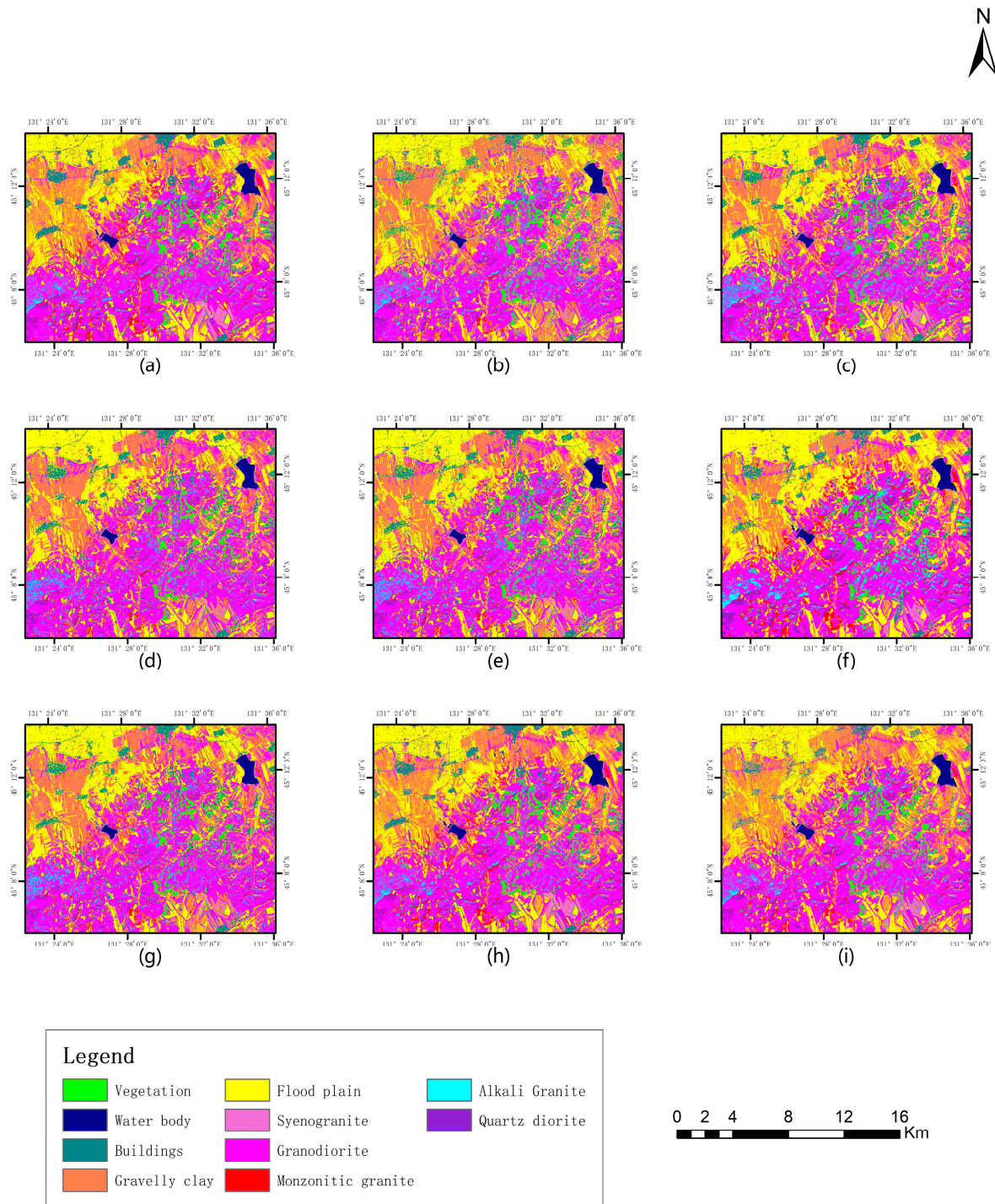


Table 5. The lithological classification accuracies of nine different datasets.

Ranking	Dataset	Overall Accuracy (%)	Kappa Coefficient
1	GF2_D	82.5311	0.7861
2	GF2_E	81.5712	0.7740
3	GF2_S	81.3125	0.7711
4	GF2_M	81.1151	0.7689
5	GF2_H	80.6045	0.7618
6	GF2_Con	79.8080	0.7521
7	GF2_V	79.3791	0.7471
8	GF2_Corr	77.1257	0.7175
9	GF2	74.6681	0.6869

Table 6 presents the producer accuracy and user accuracy for each class in the lithological classification of nine datasets. The results indicate that combining the GF2 dataset with texture can improve classification accuracy in most classes, although not all classes show improvements. For instance, in the Granodiorite class, the producer accuracy slightly decreases regardless of the texture combination, suggesting the misclassification of some Granodiorite pixels into other classes. Among these datasets, GF2_D demonstrates higher accuracy in the Buildings, Flood plain, and Syenogranite classes. On the other hand, GF2_M exhibits the most stable performance, with improved accuracy in all classes except for a slight decrease in producer accuracy in the Granodiorite class compared to GF2. GF2_E and GF2_S yield similar results in overall accuracy, Kappa coefficient, and accuracy of individual classes. Although GF2_Corr shows improved accuracy in certain classes compared to GF2, it has the highest number of classes with decreased accuracy compared to other texture-combined datasets.

Table 6. The lithological classification accuracies of nine different datasets for different classes.

Class Name	Accuracy (%)	GF2_D	GF2_E	GF2_S	GF2_M	GF2_H	GF2_Con	GF2_V	GF2_Corr	GF2
Vegetation	Producer accuracy	94.77	92.15	93.60	95.06	92.15	93.02	93.02	91.28	93.02
	User accuracy	99.69	100.00	100.00	100.00	100.00	100.00	100.00	99.68	99.69
Water body	Producer accuracy	100.00	99.07	98.99	100.00	99.24	100.00	100.00	100.00	100.00
	User accuracy	100.00	100.00	99.91	99.16	100.00	99.16	98.91	100.00	94.20
Buildings	Producer accuracy	81.30	76.82	75.68	57.61	74.23	76.94	71.95	48.64	37.84
	User accuracy	91.08	88.76	85.45	86.94	87.17	92.41	89.61	76.39	80.29
Gravelly clay	Producer accuracy	90.00	93.15	93.08	87.26	92.40	80.96	81.44	94.32	78.49
	User accuracy	87.83	83.23	83.53	84.93	83.17	80.74	81.83	76.04	74.13
Flood plain	Producer accuracy	88.39	87.83	86.89	87.44	86.53	80.59	80.53	85.45	81.05
	User accuracy	82.32	82.28	81.12	85.00	81.03	85.44	85.26	76.36	77.85
Syenogranite	Producer accuracy	68.77	53.16	53.95	76.09	51.98	79.25	81.03	27.87	63.83
	User accuracy	95.34	87.06	86.94	61.40	87.96	70.23	68.22	81.03	60.15
Granodiorite	Producer accuracy	85.40	85.86	85.15	87.94	85.75	88.12	87.65	87.35	88.54
	User accuracy	78.86	78.26	78.82	78.46	77.32	74.95	74.95	75.76	72.23
Monzonitic granite	Producer accuracy	46.55	41.22	42.41	73.77	41.42	62.13	61.93	44.58	54.64
	User accuracy	73.75	75.72	78.75	73.48	76.92	58.55	58.47	84.96	60.75
Alkali granite	Producer accuracy	53.28	51.44	55.47	39.13	50.86	35.33	36.82	41.89	34.41
	User accuracy	56.81	60.08	61.17	52.88	56.74	54.72	55.56	51.85	49.92
Quartz diorite	Producer accuracy	60.71	64.10	63.02	71.19	58.40	52.54	54.24	59.17	51.16
	User accuracy	67.81	65.72	65.76	74.64	64.46	66.09	63.88	65.53	67.34

For the Buildings, Gravelly clay, Flood plain, and Alkali granite classes, combining the GF2 dataset with different textures generally leads to noticeable improvements in both producer and user accuracy. For the Syenogranite, Granodiorite, and Monzonitic granite classes, user accuracy generally improves in different texture-combined datasets, while producer accuracy tends to decrease in most cases. Additionally, except for a slight decrease in user accuracy for the Quartz diorite class in most texture-combined datasets, the user accuracy improves generally for other classes after combining textures.

3.3. Lithological Classification Based on Different Texture Combinations

Table 7 shows the overall accuracy and Kappa coefficient of rock classification based on 28 dual-texture combination datasets. The results indicate that dual-texture overlay generally achieves better classification accuracy than single texture. It is observed that datasets with Mean texture have the highest accuracy ranking, indicating that Mean texture has an advantage in multi-texture overlay. Entropy and Second Moment generally perform well in multiple-texture overlays, consistent with their performance in single-texture analysis. However, the combination of Entropy and Second Moment results in poor performance for the GF2_E_S (81.4555%) dataset, even lower than the GF2_E (81.5712%), indicating that the combination of these two textures does not work well. The combination including Dissimilarity, except with Mean, reduces the accuracy compared to using a single Dissimilarity texture, indicating the poor performance of Dissimilarity in texture combinations. Despite the poor performance of Dissimilarity in texture combinations, its high accuracy in single texture makes the ranking of multi-texture combinations not low.

Table 7. The lithological classification accuracies of 28 different datasets.

Ranking	Dataset	Overall Accuracy (%)	Kappa Coefficient
1	GF2_E_M	87.1741	0.8441
2	GF2_M_S	86.9766	0.8418
3	GF2_D_M	86.5069	0.8357
4	GF2_H_M	86.3435	0.8338
5	GF2_Corr_M	84.3488	0.8089
6	GF2_Con_M	83.6000	0.7995
7	GF2_M_V	83.0758	0.7930
8	GF2_D_V	82.2724	0.7828
9	GF2_Con_D	82.1431	0.7812
10	GF2_Corr_D	82.0546	0.7801
11	GF2_Corr_E	81.9865	0.7791
12	GF2_D_S	81.9184	0.7784
13	GF2_D_E	81.8844	0.7779
14	GF2_Corr_H	81.8776	0.7772
15	GF2_E_H	81.6938	0.7756
16	GF2_Corr_S	81.6325	0.7748
17	GF2_E_S	81.4555	0.7725
18	GF2_Con_E	81.3602	0.7713
19	GF2_D_H	81.3262	0.7708
20	GF2_Con_S	81.2717	0.7704
21	GF2_H_S	81.2649	0.7701
22	GF2_E_V	81.0675	0.7676
23	GF2_S_V	80.8224	0.7649
24	GF2_Con_H	80.5909	0.7616
25	GF2_H_V	80.4684	0.7602
26	GF2_Con_Corr	80.2641	0.7569
27	GF2_Con_V	79.9033	0.7536
28	GF2_Corr_V	79.6378	0.7491

Contrast, Homogeneity, and Variance textures show poor performance in dual-texture overlays, generally ranking lower, and often even lower than individual texture datasets, such as GF2_H_V, GF2_Con_H, and GF2_S_V. Correlation, although having the worst performance in the single-texture dataset, surprisingly performs well in the dual-texture overlay dataset. Except for the GF2_Corr_D dataset, classification accuracy improves compared to a single texture. Next, we will try to combine more textures and select five textures: Correlation, Dissimilarity, Entropy, Second Moment, and Mean for further research of triple, quadruple, and quintuple texture combinations.

The lithology was classified based on the datasets with triple, quadruple, and quintuple textures obtained from combinations of Correlation, Dissimilarity, Entropy, Second Moment, and Mean using the SVM classification method. Among these datasets,

GF2_Corr_E_M, GF2_Corr_D_E_M, and GF2_Corr_D_E_M_S showed the highest accuracy for the triple, quadruple, and quintuple texture datasets, respectively, with their classification results shown in Figure 6. It was observed that the classification results of the three datasets were very similar. Table 8 compares the overall accuracy and Kappa coefficient of the 16 different multiple-texture combination datasets for lithological classification. The results indicated that there was little difference in the accuracy of the datasets with the best performance among the triple, quadruple, and quintuple texture datasets, namely GF2_Corr_E_M (87.8889%), GF2_Corr_D_E_M (88.5220%), and GF2_Corr_D_E_M_S (88.6037%). The dataset with the highest overall accuracy was GF2_Corr_D_E_M_S (88.6037%), which combined all five textures. In addition, the accuracy of the datasets with four textures, such as GF2_Corr_D_M_S (88.4403%), GF2_Corr_E_M_S (88.2157%), and GF2_D_E_M_S (88.0795%), were not significantly different from that of GF2_Corr_D_E_M_S (88.6037%). However, the overall accuracy of the dataset without incorporating the Mean texture, GF2_Corr_D_E_S (82.3678%), was relatively low, indicating that Mean plays a critical role in improving classification accuracy.

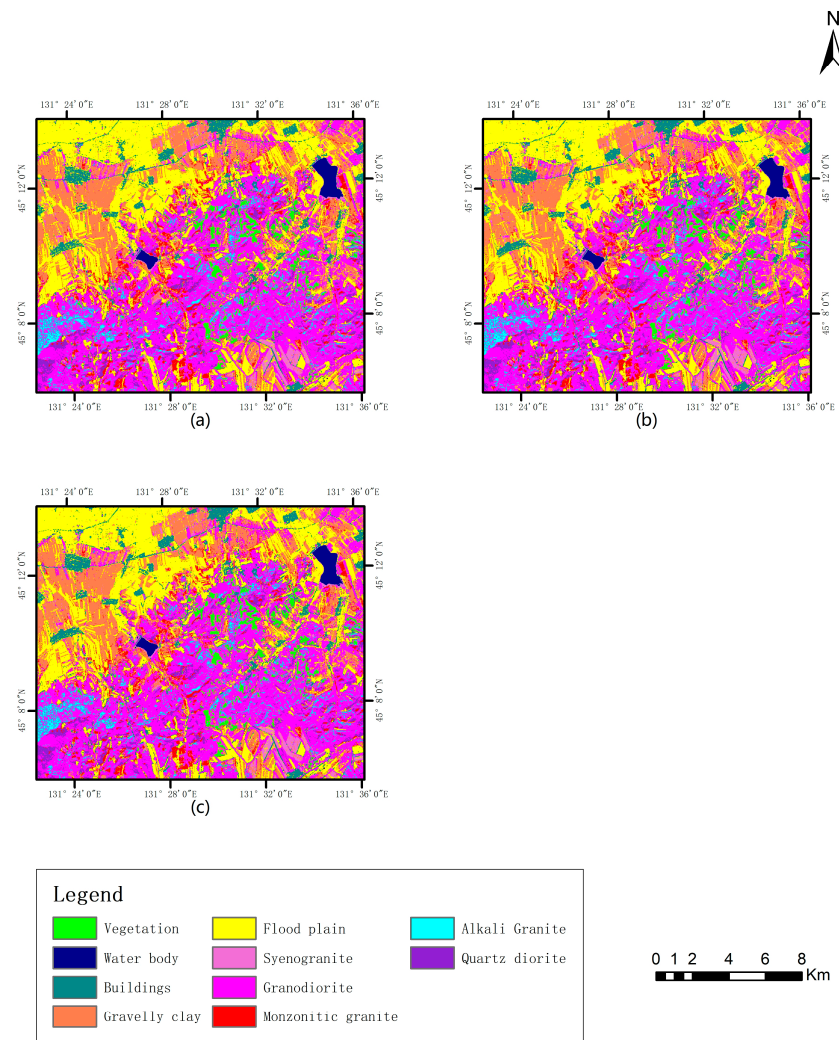


Figure 6. The lithological classification of three different datasets. (a) GF2_Corr_E_M; (b) GF2_Corr_D_E_M; (c) GF2_Corr_D_E_M_S.

Table 8. The lithological classification accuracies of 16 different datasets.

Ranking	Dataset	Overall Accuracy (%)	Kappa Coefficient
1	GF2_Corr_D_E_M_S	88.6037	0.8615
2	GF2_Corr_D_E_M	88.5220	0.8605
3	GF2_Corr_D_M_S	88.4403	0.8596
4	GF2_Corr_E_M_S	88.2157	0.8568
5	GF2_D_E_M_S	88.0795	0.8552
6	GF2_Corr_E_M	87.8889	0.8529
7	GF2_Corr_M_S	87.8685	0.8527
8	GF2_D_E_M	87.8685	0.8526
9	GF2_D_M_S	87.7323	0.8510
10	GF2_E_M_S	87.6438	0.8499
11	GF2_Corr_D_M	87.0175	0.8419
12	GF2_Corr_D_S	82.4631	0.7850
13	GF2_Corr_D_E_S	82.3678	0.7839
14	GF2_Corr_D_E	82.2793	0.7827
15	GF2_D_E_S	82.0069	0.7792
16	GF2_Corr_E_S	81.9525	0.7787

Although with an increasing number of layers, the improvement in the highest accuracy gradually becomes weaker, the number of texture overlays seems to be positively correlated with classification accuracy. To verify whether this relationship still exists when more layers are added, we will try to add more layers.

Table 9 compares the overall accuracy and Kappa coefficient of seven different multiple-texture combination datasets for lithological classification. The results indicate that adding more textures does not always lead to better accuracy. Except for the GF2_Corr_D_E_H_M_S (88.6922%) dataset, which had slightly higher accuracy than GF2_Corr_D_E_M_S (88.6037%), the accuracy of the other datasets decreased as more textures were added and was lower than GF2_Corr_D_E_M_S. However, the poor performance of the texture combinations of Contrast, Homogeneity, and Variance themselves may be one of the reasons for the decrease in overall accuracy. Examples of GF2_Con (79.8080%), GF2_V (79.3791%), and GF2_Con_V (79.9033%) show that using the combination of Contrast + Variance produces higher accuracy than using either individually. However, the results of GF2_Con_Corr_D_E_M_S (88.4335%), GF2_Corr_D_E_M_S_V (88.4267%), and GF2_Con_Corr_D_E_M_S_V (88.1544%) indicate that the accuracy after combining Contrast + Variance was lower than using either individually, suggesting that the main reason for the decrease in accuracy was due to stacking too many layers of data. In summary, the number of layers of stacked textures needs to be controlled within a reasonable range, as exceeding this range can result in a decline in performance.

Table 9. The lithological classification accuracies of seven different datasets.

Ranking	Dataset	Overall Accuracy (%)	Kappa Coefficient
1	GF2_Corr_D_E_H_M_S	88.6922	0.8626
2	GF2_Corr_D_E_H_M_S_V	88.4403	0.8595
3	GF2_Con_Corr_D_E_M_S	88.4335	0.8594
4	GF2_Corr_D_E_M_S_V	88.4267	0.8593
5	GF2_Con_Corr_D_E_H_M_S	88.4131	0.8592
6	GF2_Con_Corr_D_E_H_M_S_V	88.1612	0.8561
7	GF2_Con_Corr_D_E_M_S_V	88.1544	0.8560

3.4. Lithological Classification Based on PCA and ICA Datasets

PCA and ICA were used to process GF-2 data, resulting in PCA and ICA datasets. The texture combination experiment was conducted using the PCA and ICA datasets as replacements for the original GF-2 data, evaluating the effects of PCA and ICA on lithological classification and the performance of different combination methods.

Figure 7 shows the results of lithological classification using the support vector machine classification method for PCA, ICA, and GF2. Table 10 compares the overall accuracy and Kappa coefficients of lithological classification for the three datasets. The results indicate that, compared to GF2 (74.6681%), both PCA (75.6553%) and ICA (74.7634%) increased the classification accuracy. This suggests that PCA and ICA processing indeed aid lithological classification.

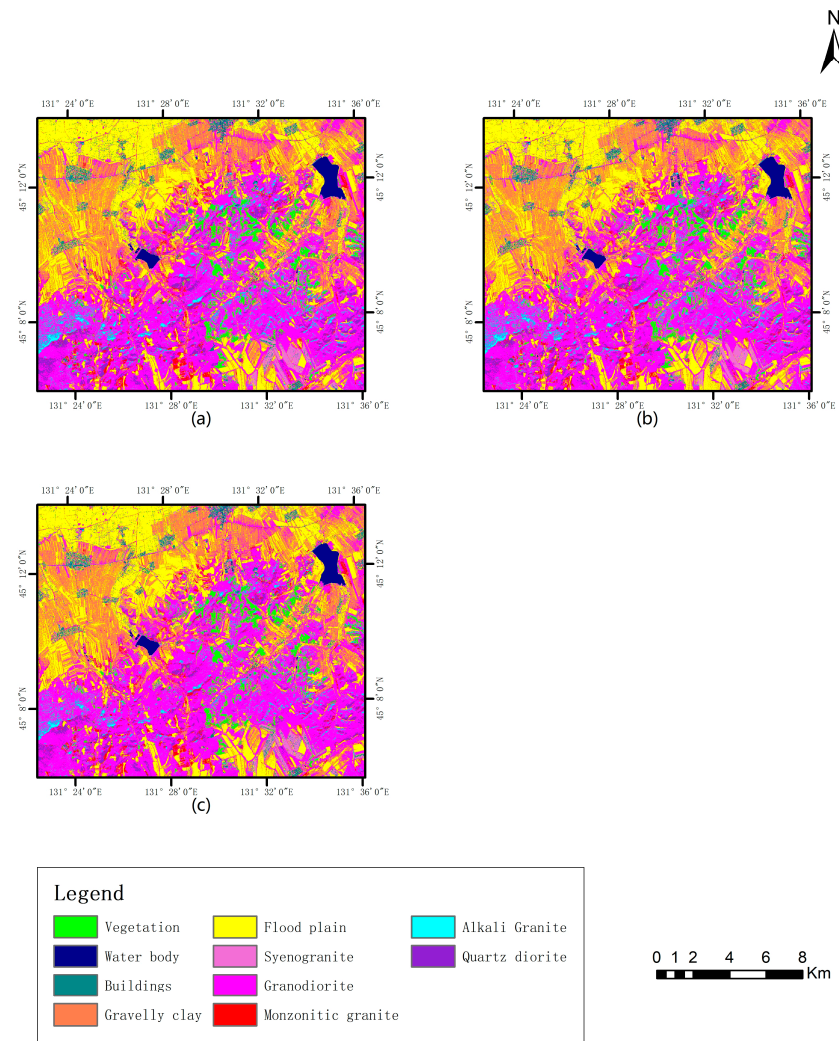


Figure 7. The lithological classification of different datasets. (a) PCA; (b) ICA; (c) GF2.

Table 10. The lithological classification accuracies of different datasets.

Processing Method	Overall Accuracy (%)	Kappa Coefficient
PCA	75.6553	0.7015
ICA	74.7634	0.6891
GF2	74.6681	0.6869

Figure 8 shows the results of lithological classification using the support vector machine classification method for different texture datasets processed by PCA. Figure 9 shows the corresponding results for ICA. Table 11 compares the overall accuracy of lithological classification for different datasets of GF2, PCA, and ICA. The results indicate that when combining textures, the dataset accuracy of both PCA and ICA is higher than that of GF2 with the corresponding textures. Although PCA alone has a higher accuracy (75.6553%) than ICA (74.7634%), when textures are combined, PCA and ICA have their respective strengths. For example, ICA_M (85.0228%) has a higher accuracy than PCA_M (83.0281%).

Additionally, unlike GF2_D, which had the highest accuracy among GF2's texture combinations, PCA_E and ICA_E had the highest accuracies in their respective texture combinations.

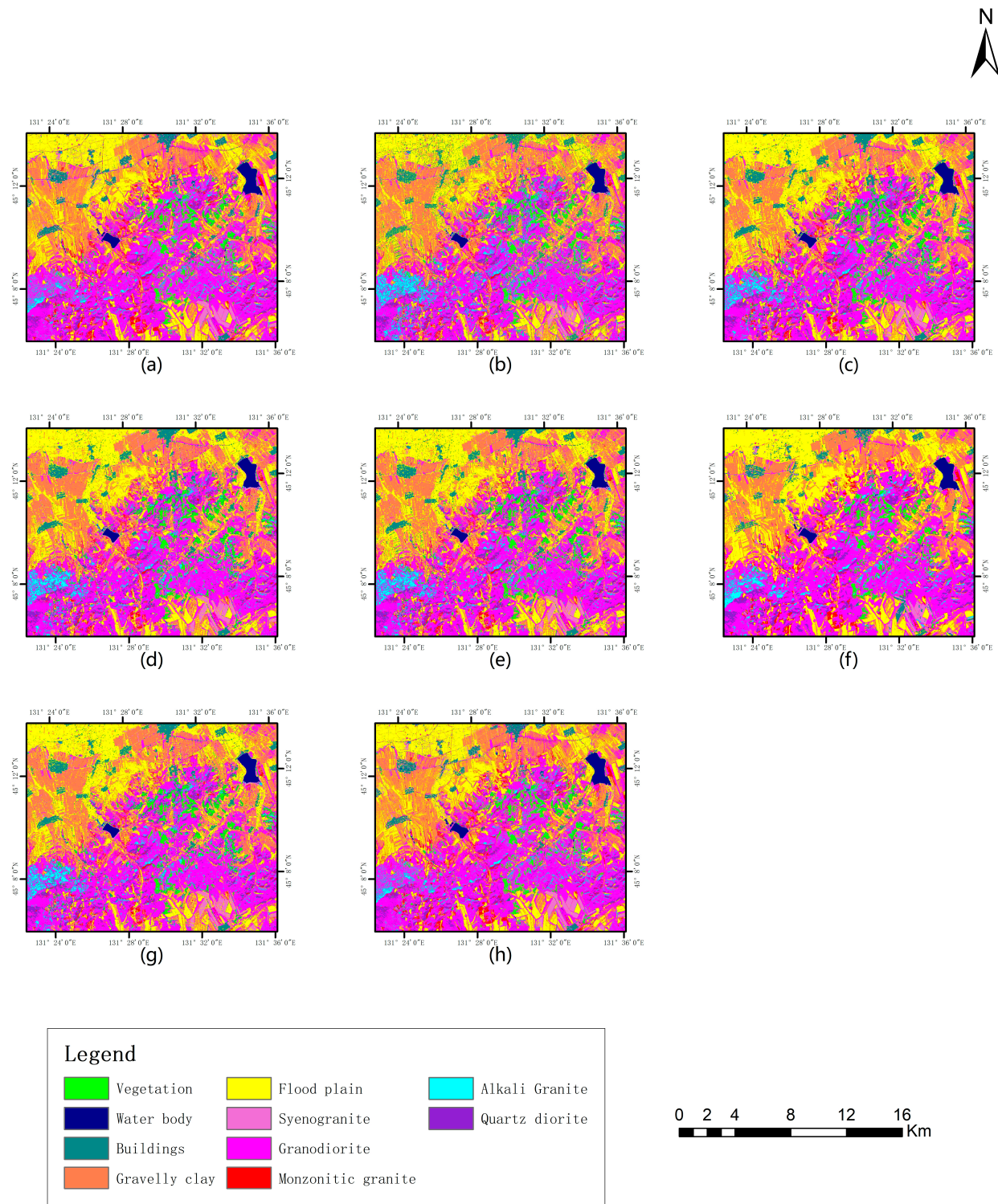


Figure 8. The lithological classification of different datasets. (a) PCA_Con; (b) PCA_Corr; (c) PCA_D; (d) PCA_E; (e) PCA_H; (f) PCA_M; (g) PCA_S; (h) PCA_V.

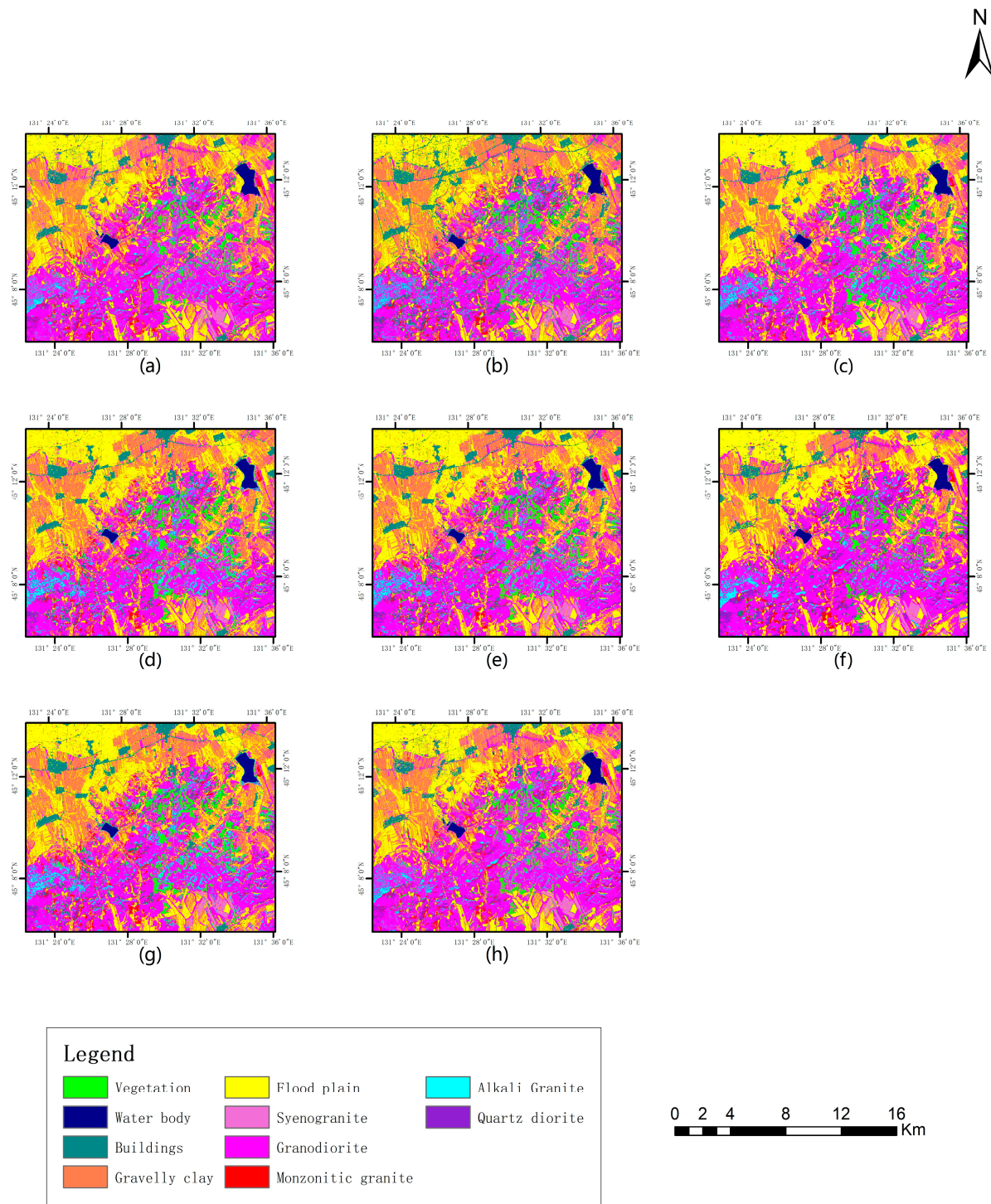


Figure 9. The lithological classification of different datasets. (a) ICA_Con; (b) ICA_Corr; (c) ICA_D; (d) ICA_E; (e) ICA_H; (f) ICA_M; (g) ICA_S; (h) ICA_V.

Table 12 compares the overall accuracy of lithological classification for different dual-texture datasets of GF2, PCA, and ICA. Due to the poor performance of Contrast and Variance texture combinations, they were not included in this experiment. The results show that the datasets of both PCA and ICA perform better than that of GF2, with PCA_E_M (90.6120%) having the highest accuracy among all 45 datasets. Generally, dataset performance was slightly better for PCA than ICA, particularly for high-accuracy combinations such as PCA_E_M (90.6120%). In contrast, the feature of ICA datasets lies in their con-

sistency, as there is not much variation between the performance of different texture combinations.

Table 11. The comparison of lithological classification accuracies of different datasets.

Dataset	Overall Accuracy (%)	Dataset	Overall Accuracy (%)	Dataset	Overall Accuracy (%)
GF2_Con	79.8080	PCA_Con	79.9850	ICA_Con	79.8693
GF2_Corr	77.1257	PCA_Corr	80.8632	ICA_Corr	81.0130
GF2_D	82.5311	PCA_D	84.9888	ICA_D	85.1113
GF2_E	81.5712	PCA_E	86.5546	ICA_E	85.9419
GF2_H	80.6045	PCA_H	85.5810	ICA_H	84.7369
GF2_M	81.1151	PCA_M	83.0281	ICA_M	85.0228
GF2_S	81.3125	PCA_S	86.0099	ICA_S	85.7649
GF2_V	79.3791	PCA_V	79.6923	ICA_V	80.1620

Table 12. The comparison of lithological classification accuracies of 45 different datasets.

Dataset	Overall Accuracy (%)	Dataset	Overall Accuracy (%)	Dataset	Overall Accuracy (%)
GF2_Corr_D	82.0546	PCA_Corr_D	85.7308	ICA_Corr_D	86.0372
GF2_Corr_E	81.9865	PCA_Corr_E	86.8950	ICA_Corr_E	86.3912
GF2_Corr_H	81.8776	PCA_Corr_H	86.6431	ICA_Corr_H	85.9078
GF2_Corr_M	84.3488	PCA_Corr_M	86.7248	ICA_Corr_M	85.9010
GF2_Corr_S	81.6325	PCA_Corr_S	86.7792	ICA_Corr_S	86.3095
GF2_D_E	81.8844	PCA_D_E	86.1801	ICA_D_E	86.0916
GF2_D_H	81.3262	PCA_D_H	85.2747	ICA_D_H	84.8322
GF2_D_M	86.5069	PCA_D_M	88.7943	ICA_D_M	88.2157
GF2_D_S	81.9184	PCA_D_S	85.8057	ICA_D_S	86.3163
GF2_E_H	81.6938	PCA_E_H	86.1938	ICA_E_H	86.0440
GF2_E_M	87.1741	PCA_E_M	90.6120	ICA_E_M	88.8216
GF2_E_S	81.4555	PCA_E_S	86.1189	ICA_E_S	85.6015
GF2_H_M	86.3435	PCA_H_M	89.4887	ICA_H_M	88.2225
GF2_H_S	81.2649	PCA_H_S	85.9078	ICA_H_S	86.1189
GF2_M_S	86.9766	PCA_M_S	90.4691	ICA_M_S	88.6786

Figure 10 and Table 13 present a comparison of the overall accuracies for lithological classification using different multiple-texture datasets, including GF2, PCA, and ICA. Undoubtedly, both the PCA and ICA datasets still outperform the GF2 dataset, with the PCA dataset consistently achieving higher overall accuracy compared to the ICA dataset. PCA_Corr_E_M (91.2860%) performs the best among all triple-texture combination datasets, while PCA_Corr_E_M_S (91.4562%) achieves the best performance among all quadruple-texture combination datasets. The slight difference between them indicates that the effect of texture combination on classification accuracy is small after triple combination. However, the accuracy of the quintuple texture combination PCA_Corr_D_E_M_S (91.3813%) decreases instead of increasing compared to PCA_Corr_E_M_S (91.4562%), which suggests that excessive texture combination not only increases computational complexity but also leads to reduced accuracy. Furthermore, the poor performance of Dissimilarity texture in the PCA dataset and the negative impact caused by its combination with other textures are observed. Continuing to combine textures on the basis of the quintuple texture combination will further demonstrate the drawbacks of excessive texture combination.

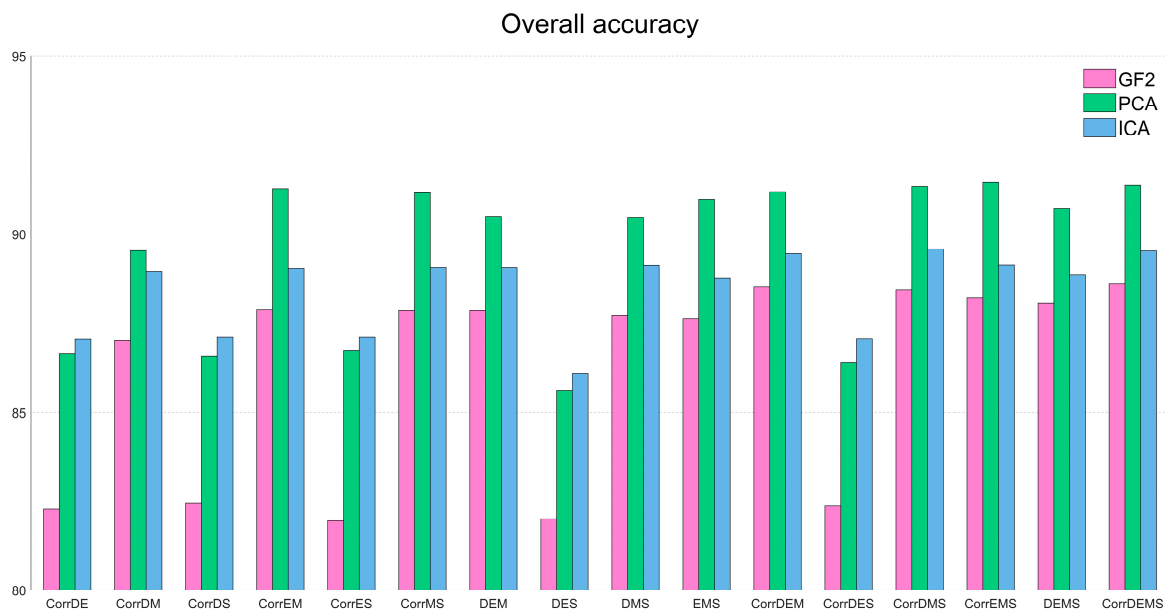


Figure 10. Overall accuracy of 48 different datasets.

Table 13. The comparison of lithological classification accuracies of 48 different datasets.

Dataset	Overall Accuracy (%)	Dataset	Overall Accuracy (%)	Dataset	Overall Accuracy (%)
GF2_Corr_D_E	82.2793	PCA_Corr_D_E	86.6431	ICA_Corr_D_E	87.0515
GF2_Corr_D_M	87.0175	PCA_Corr_D_M	89.5568	ICA_Corr_D_M	88.9577
GF2_Corr_D_S	82.4631	PCA_Corr_D_S	86.5818	ICA_Corr_D_S	87.1060
GF2_Corr_E_M	87.8889	PCA_Corr_E_M	91.2860	ICA_Corr_E_M	89.0394
GF2_Corr_E_S	81.9525	PCA_Corr_E_S	86.7248	ICA_Corr_E_S	87.1060
GF2_Corr_M_S	87.8685	PCA_Corr_M_S	91.1771	ICA_Corr_M_S	89.0666
GF2_D_E_M	87.8685	PCA_D_E_M	90.5031	ICA_D_E_M	89.0666
GF2_D_E_S	82.0069	PCA_D_E_S	85.6219	ICA_D_E_S	86.1052
GF2_D_M_S	87.7323	PCA_D_M_S	90.4759	ICA_D_M_S	89.1279
GF2_E_M_S	87.6438	PCA_E_M_S	90.9865	ICA_E_M_S	88.7603
GF2_Corr_D_E_M	88.5220	PCA_Corr_D_E_M	91.2043	ICA_Corr_D_E_M	89.4683
GF2_Corr_D_E_S	82.3678	PCA_Corr_D_E_S	86.4184	ICA_Corr_D_E_S	87.0583
GF2_Corr_D_M_S	88.4403	PCA_Corr_D_M_S	91.3473	ICA_Corr_D_M_S	89.5977
GF2_Corr_E_M_S	88.2157	PCA_Corr_E_M_S	91.4562	ICA_Corr_E_M_S	89.1347
GF2_D_E_M_S	88.0795	PCA_D_E_M_S	90.7209	ICA_D_E_M_S	88.8692
GF2_Corr_D_E_M_S	88.6037	PCA_Corr_D_E_M_S	91.3813	ICA_Corr_D_E_M_S	89.5432

Figure 11 and Table 14 present a comparison of the overall accuracies for lithological classification using different multiple-texture datasets, including GF2, PCA, and ICA. The results demonstrate that the accuracy of various datasets has stabilized after combining multiple textures. All PCA datasets in the table have lower accuracy than the quintuple texture combination PCA_Corr_D_E_M_S (91.3813%) mentioned in previous paragraphs, while the GF2 and ICA datasets, except for GF2_Corr_D_E_H_M_S (88.6922%) and ICA_Corr_D_E_H_M_S (89.6385%), have lower accuracy compared to their corresponding GF2_Corr_D_E_M_S (88.6037%) and ICA_Corr_D_E_M_S (89.5432%). Generally speaking, the number of texture combinations needs to be controlled within a reasonable range.

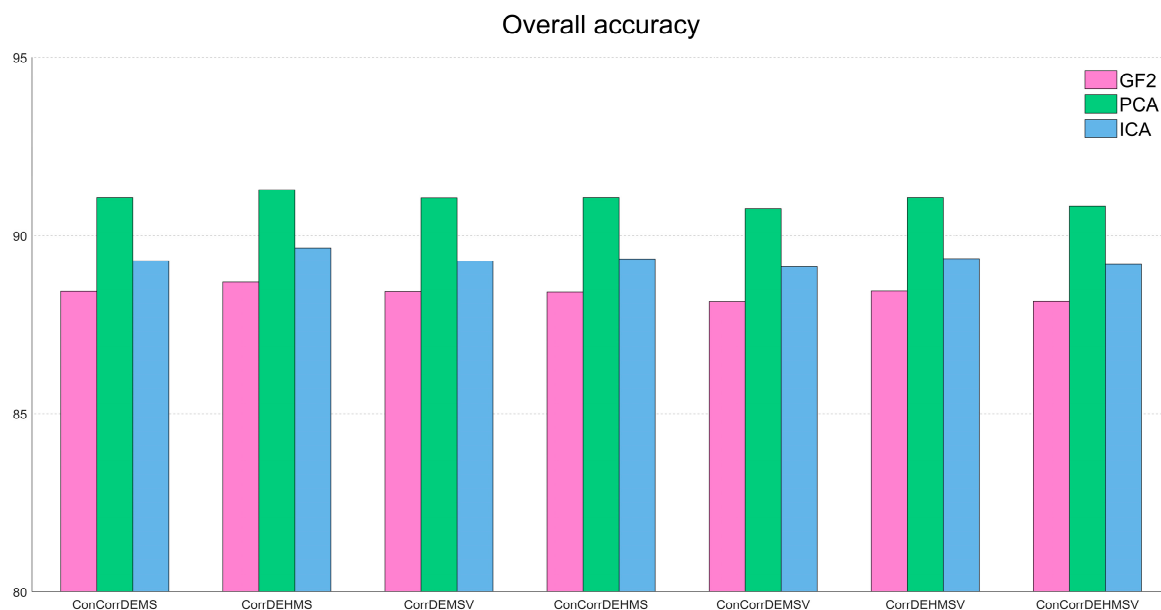


Figure 11. Overall accuracy of 21 different datasets.

Table 14. The comparison of lithological classification accuracies of 21 different datasets.

Dataset	Overall Accuracy (%)	Dataset	Overall Accuracy (%)	Dataset	Overall Accuracy (%)
GF2_Con_Corr_D_E_M_S	88.4335	PCA_Con_Corr_D_E_M_S	91.0613	ICA_Con_Corr_D_E_M_S	89.2845
GF2_Con_Corr_D_E_H_M_S	88.6922	PCA_Con_Corr_D_E_H_M_S	91.2860	ICA_Con_Corr_D_E_H_M_S	89.6385
GF2_Con_Corr_D_E_M_S_V	88.4267	PCA_Con_Corr_D_E_M_S_V	91.0545	ICA_Con_Corr_D_E_M_S_V	89.2777
GF2_Con_Corr_D_E_H_M_S	88.4131	PCA_Con_Corr_D_E_H_M_S	91.0613	ICA_Con_Corr_D_E_H_M_S	89.3390
GF2_Con_Corr_D_E_M_S_V	88.1544	PCA_Con_Corr_D_E_M_S_V	90.7414	ICA_Con_Corr_D_E_M_S_V	89.1211
GF2_Con_Corr_D_E_H_M_S_V	88.4403	PCA_Con_Corr_D_E_H_M_S_V	91.0613	ICA_Con_Corr_D_E_H_M_S_V	89.3458
GF2_Con_Corr_D_E_H_M_S_V	88.1612	PCA_Con_Corr_D_E_H_M_S_V	90.8094	ICA_Con_Corr_D_E_H_M_S_V	89.1824

Table 15 presents the relevant results of the accuracy assessment for the PCA_Corr_E_M dataset mentioned earlier using geological maps. However, the classification accuracy using geological maps is lower compared to using testing samples. This could be attributed to the various limitations associated with digitized geological maps, leading to some uncertainty in the information. In contrast, testing samples provide more accurate information. Furthermore, considering the remote sensing limitations discussed earlier, this level of accuracy is reasonable.

Table 15. The classification accuracies of PCA_Corr_E_M dataset using geological map.

Overall Accuracy (%)	56.8237	
Kappa coefficient	0.4146	
Class name	Producer accuracy (%)	User accuracy (%)
Water body	89.97	98.37
Gravelly clay	44.76	62.91
Flood plain	70.04	44.90
Syenogranite	28.82	45.64
Granodiorite	60.84	75.60
Monzonitic granite	45.36	14.39
Alkali granite	50.08	35.05
Quartz diorite	45.53	20.99

4. Discussion

In this study, different methods were used to classify lithology with GF-2 data, and the results showed that the support vector machine had the highest overall accuracy. Therefore, support vector machine was used for further research.

This study investigates the impact of eight GLCM-defined texture indices on lithological classification. The experimental findings demonstrate the superiority of datasets incorporating arbitrary texture overlays on GF-2 data over those using GF-2 data alone. This suggests a positive influence of all eight texture indices on lithological classification. Notably, the GF2_D dataset exhibited the highest accuracy (82.5311%) due to its sensitivity to grayscale changes. For instance, the Dissimilarity index effectively identifies the Buildings class by leveraging the distinctive grayscale variations associated with artificial structures. Compared to other datasets, GF2_D displayed higher producer and user accuracy for the Buildings class, except for the user accuracy of the GF2_Con dataset. This discrepancy arises from the exponential weighting employed by the Contrast index, making it more responsive to grayscale changes and thereby increasing user accuracy. Nevertheless, excessive sensitivity to grayscale variations can result in subpar classification performance for most classes, thus explaining the relatively low overall accuracy of the GF2_Con dataset.

The Entropy and Second Moment indices serve as complementary measures to assess the regularity of grayscale distribution, albeit from contrasting perspectives. Consequently, GF2_E and GF2_S exhibit consistent overall and individual class accuracy. Among them, GF2_M demonstrates the most stable performance, displaying a stable improvement in classification accuracy across various classes. This stability can be attributed to the smoothing filtering effect of the Mean index, which effectively eliminates noise and yields stable classification enhancement. On the other hand, the Homogeneity and Variance indices reflect grayscale homogeneity and dispersion, respectively. Unlike Entropy, they are not sensitive to grayscale distribution, resulting in the possibility of an image with a high Variance value having a regular grayscale distribution. Experimental results validate the superior classification performance of GF2_E compared to GF2_H and GF2_V. The Correlation index evaluates the linear correlation of grayscale in images, but its direct impact on classification appears to be insignificant, resulting in the poorest performance observed for GF2_Corr.

Considering the distinctive characteristics of each texture index, their combination is expected to enhance classification performance. The research findings demonstrate that dual-texture combinations generally outperform single textures in terms of classification accuracy. Combining the Mean index, which effectively eliminates noise, with other texture indices resulted in higher accuracy datasets. Both the Entropy and Second Moment indices exhibited strong performance in texture combinations, except for the GF2_E_S combination, which suffered from mutual interference stemming from their contrasting perspectives on grayscale distribution.

On the other hand, while the Correlation index did not demonstrate satisfactory performance when used alone, it exhibited suitable results in dual-texture combinations. In contrast, the Dissimilarity index showed excellent performance when used alone, but its effectiveness in dual-texture combinations varied depending on the case. As for the Homogeneity, Variance, and Contrast indices, neither their individual performance nor their performance in combination met the desired standards. Therefore, these three indices were not included in further texture combinations.

Based on the experimental results, incorporating the Mean metric proves essential to enhance classification accuracy. The accuracy of the triple-texture dataset containing Mean exhibits minimal variation, while the accuracy of the quadruple-texture dataset, also including Mean, demonstrates stable performance. When the number of texture combinations is limited to five, there seems to be a positive correlation between the number of combinations and accuracy. However, beyond five combinations, as the number of textures increases, the accuracy of the dataset shows a downward trend. This decline is known as the “curse of dimensionality”, where classification performance initially improves with increasing dimensionality but eventually deteriorates due to overfitting caused by excessive dimensions [55,56]. To mitigate overfitting, increasing the number of training datasets is effective. However, as the dimensionality increases, the required number of

training datasets also increases rapidly while the amount of data is limited. Consequently, selecting an appropriate number of layers is crucial in practical classification scenarios.

The paper also explores the impact of PCA and ICA on lithological classification, evaluating their effectiveness in combination with different textures. Experimental findings reveal that datasets combining PCA or ICA with textures achieve higher classification accuracy compared to those combining GF2 with corresponding textures. Among these approaches, PCA displays superior performance in high-accuracy texture combination datasets compared to ICA. ICA has the characteristic that accuracy changes little between various combinations.

Multispectral data are typically collected to acquire spectral information in specific wavelength bands, which reflect the fundamental spectral characteristics of objects on the Earth's surface. Through the analysis and pattern recognition of spectral information, it is possible to classify and identify different types of rocks. Multispectral sensors are cost-effective and have higher spatial resolution, making data acquisition and processing relatively straightforward. As a result, multispectral data finds wide applications in remote sensing-based lithological classification and has reached a relatively mature stage of development [57–66]. However, there is still untapped potential for further advancements in the use of multispectral data in lithological classification. With continuous improvements in remote sensing technology and image processing algorithms, the application of multispectral data is becoming more accurate and reliable. For instance, the application of more suitable machine learning methods can enhance the accuracy of lithological classification results. Additionally, combining multispectral data with data processed through different algorithms can further increase the value of multispectral data in lithological classification.

The integration of multispectral data with texture data, PCA data, and ICA data for lithological classification is rare in previous studies. In this research, the combination of multispectral data, texture data, PCA data, and ICA data is explored, and the application value of their integration in lithological classification is investigated. The comprehensive utilization of multiple data sources contributes to improved accuracy and reliability in lithological classification, providing more reliable information support for geological research and resource development. Due to experimental conditions and time limitations, only one study area was selected, and only a subset of texture defined by GLCM was used, which limits the scope of our study.

Despite being in a relatively mature stage of development, there are still new trends emerging in the remote sensing lithological classification of multispectral data. For instance, in the future, we can further integrate data from other sensors, such as radar, to extract additional feature information and enhance the discriminative ability of multispectral data in lithological classification. Additionally, the adoption of high-resolution image decomposition techniques can be employed to decompose and reconstruct multispectral data, aiming to achieve results and accuracy closer to that of hyperspectral data.

5. Conclusions

This study applies a support vector machine to classify lithology in the research area of Jixi City, Heilongjiang Province, China, using GF-2 data. The research aims to evaluate the impact of different texture indices and combinations on lithological classification. Additionally, the effects of combining PCA and ICA with textures on lithological classification were investigated. Based on the experimental results, the following conclusions were drawn:

- (1) In this study, the support vector machine was most suitable for classifying GF-2 data for lithological classification. In addition to this, neural network classification was superior to minimum distance classification and maximum likelihood classification.
- (2) When GF-2 data were combined with single-texture data, the accuracy of datasets combining GF-2 data with any texture generally surpassed that of using GF-2 data alone. Notably, the GF2_D(82.5311%) dataset incorporating the Dissimilarity index achieved the highest overall accuracy, while the GF2_M(81.1151%) dataset employing the Mean index demonstrated stable accuracy improvement for each class.

- (3) The combination of GF-2 data with multiple textures generally resulted in higher classification accuracy compared to using a single texture. The Mean index played a pivotal role in enhancing dataset accuracy. However, excessive texture overlap led to reduced classification accuracy. Considering the performance and limitations of training datasets, utilizing a triple-texture dataset is a reasonable option. In the triple-texture dataset, the GF2_Corr_E_M dataset had the highest accuracy of 87.8889%.
- (4) Both PCA and ICA had a positive effect on the accuracy of lithological classification, with PCA performing better than ICA in high-accuracy texture combination datasets. The accuracy of PCA_Corr_E_M (91.2860%) improved by 3.3971% relative to GF2_Corr_E_M (87.8889%).

Through the integration of multiple data sources, this study holds the potential to enhance the accuracy of lithological classification. Texture data can provide information about the morphological characteristics of rock surfaces, while PCA and ICA can extract the principal and independent components from the original data, further enhancing the feasibility and effectiveness of classification. Lithological classification plays a vital role in geological investigations and resource exploration. By comprehensively utilizing diverse data sources for lithological classification, it can provide more accurate and comprehensive geological information for geological investigations and resource exploration, offering a scientific basis for related decisions.

This article only studied the effects of textures defined by GLCM on lithological classification. In future research, it will be possible to compare the effects of different definitions of texture on lithological classification. Moreover, GF-2 data can be combined with DEM data, gravity-magnetic data, and other multispectral data for further study on the impact of different combinations on lithological classification.

Author Contributions: Conceptualization, T.C. and C.Y.; methodology, T.C. and C.Y.; software, T.C.; validation, T.C.; formal analysis, T.C.; investigation, C.Y.; resources, C.Y. and L.H.; data curation, T.C. and C.Y.; writing—original draft preparation, T.C.; writing—review and editing, T.C., C.Y., L.H., and S.G.; supervision, C.Y. and L.H.; All authors have read and agreed to the published version of the manuscript.

Funding: This research was funded by the Natural Science Foundation of China, grant numbers 42130805 and 42074154, and the China Geological Survey, grant numbers DD20211579.

Data Availability Statement: The GF-2 satellite data were downloaded from the China Centre for Resources Satellite Data and Application (<https://data.cresda.cn/#/2dMap> (accessed on 25 October 2020)).

Acknowledgments: The authors thank all those students and teachers from Jilin University who actively participated in the field and laboratory work. The authors thank the support of Chunhai Li in editing the paper. The authors thank the China Centre for Resources Satellite Data and Application (<https://data.cresda.cn/#/2dMap> (accessed on 25 October 2020)) (e-mail: service@cresda.com and cresda_yxb@spacechina.com) for providing the GF-2 satellite data.

Conflicts of Interest: The authors declare no conflict of interest.

References

1. Masoumi, F.; Eslamkish, T.; Abkar, A.A.; Honarmand, M.; Harris, J.R. Integration of Spectral, Thermal, and Textural Features of ASTER Data Using Random Forests Classification for Lithological Mapping. *J. Afr. Earth Sci.* **2017**, *129*, 445–457. [[CrossRef](#)]
2. Alexandridis, T.K.; Topaloglou, C.A.; Lazaridou, E.; Zalidis, G.C. The Performance of Satellite Images in Mapping Aquacultures. *Ocean Coast. Manag.* **2008**, *51*, 638–644. [[CrossRef](#)]
3. Li, X.; Damen, M.C.J. Coastline Change Detection with Satellite Remote Sensing for Environmental Management of the Pearl River Estuary, China. *J. Mar. Syst.* **2010**, *82*, S54–S61. [[CrossRef](#)]
4. Amer, R.; Kusky, T.; Ghulam, A. Lithological Mapping in the Central Eastern Desert of Egypt Using ASTER Data. *J. Afr. Earth Sci.* **2010**, *56*, 75–82. [[CrossRef](#)]
5. Aydal, D.; Arda1, E.; Dumanlilar, Ö. Application of the Crosta Technique for Alteration Mapping of Granitoidic Rocks Using ETM+ Data: Case Study from Eastern Tauride Belt (SE Turkey). *Int. J. Remote Sens.* **2007**, *28*, 3895–3913. [[CrossRef](#)]

6. Chen, X.; Warner, T.A.; Campagna, D.J. Integrating Visible, near-Infrared and Short-Wave Infrared Hyperspectral and Multispectral Thermal Imagery for Geological Mapping at Cuprite, Nevada. *Remote Sens. Environ.* **2007**, *110*, 344–356. [[CrossRef](#)]
7. Gad, S.; Kusky, T. Lithological Mapping in the Eastern Desert of Egypt, the Barramiya Area, Using Landsat Thematic Mapper (TM). *J. Afr. Earth Sci.* **2006**, *44*, 196–202. [[CrossRef](#)]
8. Grebby, S.; Field, E.; Tansey, K. Evaluating the Use of an Object-Based Approach to Lithological Mapping in Vegetated Terrain. *Remote Sens.* **2016**, *8*, 843. [[CrossRef](#)]
9. Guo, S.; Yang, C.; He, R.; Li, Y. Improvement of Lithological Mapping Using Discrete Wavelet Transformation from Sentinel-1 SAR Data. *Remote Sens.* **2022**, *14*, 5824. [[CrossRef](#)]
10. Lu, Y.; Yang, C.; Jiang, Q. Evaluation of the Performance of Time-Series Sentinel-1 Data for Discriminating Rock Units. *Remote Sens.* **2021**, *13*, 4824. [[CrossRef](#)]
11. Ninomiya, Y.; Fu, B.; Cudahy, T.J. Detecting Lithology with Advanced Spaceborne Thermal Emission and Reflection Radiometer (ASTER) Multispectral Thermal Infrared “Radiance-at-Sensor” Data. *Remote Sens. Environ.* **2005**, *99*, 127–139. [[CrossRef](#)]
12. Pour, A.B.; Hashim, M.; Hong, J.K.; Park, Y. Lithological and Alteration Mineral Mapping in Poorly Exposed Lithologies Using Landsat-8 and ASTER Satellite Data: North-Eastern Graham Land, Antarctic Peninsula. *Ore Geol. Rev.* **2019**, *108*, 112–133. [[CrossRef](#)]
13. Pour, A.B.; Park, Y.; Park, T.-Y.S.; Hong, J.K.; Hashim, M.; Woo, J.; Ayoobi, I. Evaluation of ICA and CEM Algorithms with Landsat-8/ASTER Data for Geological Mapping in Inaccessible Regions. *Geocarto Int.* **2019**, *34*, 785–816. [[CrossRef](#)]
14. Rowan, L.C.; Mars, J.C. Lithologic Mapping in the Mountain Pass, California Area Using Advanced Spaceborne Thermal Emission and Reflection Radiometer (ASTER) Data. *Remote Sens. Environ.* **2003**, *84*, 350–366. [[CrossRef](#)]
15. Hajaj, S.; El Harti, A.; Jellouli, A.; Pour, A.B.; Mnissar Himyari, S.; Hamzaoui, A.; Hashim, M. Evaluating the Performance of Machine Learning and Deep Learning Techniques to HyMap Imagery for Lithological Mapping in a Semi-Arid Region: Case Study from Western Anti-Atlas, Morocco. *Minerals* **2023**, *13*, 766. [[CrossRef](#)]
16. Karimzadeh, S.; Tangestani, M.H. Evaluating the VNIR-SWIR Datasets of WorldView-3 for Lithological Mapping of a Metamorphic-Igneous Terrain Using Support Vector Machine Algorithm; a Case Study of Central Iran. *Adv. Space Res.* **2021**, *68*, 2421–2440. [[CrossRef](#)]
17. Shirmard, H.; Farahbakhsh, E.; Müller, R.D.; Chandra, R. A Review of Machine Learning in Processing Remote Sensing Data for Mineral Exploration. *Remote Sens. Environ.* **2022**, *268*, 112750. [[CrossRef](#)]
18. Sekandari, M.; Masoumi, I.; Pour, A.B.; Muslim, A.M.; Hossain, M.S.; Misra, A. ASTER and WorldView-3 Satellite Data for Mapping Lithology and Alteration Minerals Associated with Pb-Zn Mineralization. *Geocarto Int.* **2022**, *37*, 1782–1812. [[CrossRef](#)]
19. Zhou, Y.; Zheng, S.; An, Y.; Lai, C. ASTER VNIR-SWIR Based Lithological Mapping of Granitoids in the Western Junggar Orogen (NW Xinjiang): Improved Inputs to Random Forest Method. *Earth Space Sci.* **2023**, *10*, 2877. [[CrossRef](#)]
20. Harris, J.R.; Rogge, D.; Hitchcock, R.; Ijewliw, O.; Wright, D. Mapping Lithology in Canada’s Arctic: Application of Hyperspectral Data Using the Minimum Noise Fraction Transformation and Matched Filtering. *Can. J. Earth Sci.* **2005**, *42*, 2173–2193. [[CrossRef](#)]
21. Ge, W.; Cheng, Q.; Jing, L.; Armenakis, C.; Ding, H. Lithological Discrimination Using ASTER and Sentinel-2A in the Shibanzhong Ophiolite Complex of Beishan Orogenic in Inner Mongolia, China. *Adv. Space Res.* **2018**, *62*, 1702–1716. [[CrossRef](#)]
22. Yu, L.; Porwal, A.; Holden, E.-J.; Dentith, M.C. Towards Automatic Lithological Classification from Remote Sensing Data Using Support Vector Machines. *Comput. Geosci.* **2012**, *45*, 229–239. [[CrossRef](#)]
23. Weszka, J.S.; Dyer, C.R.; Rosenfeld, A. A Comparative Study of Texture Measures for Terrain Classification. *IEEE Trans. Syst. Man Cybern.* **1976**, *SMC-6*, 269–285. [[CrossRef](#)]
24. Connors, R.W.; Harlow, C.A. A Theoretical Comparison of Texture Algorithms. *IEEE Trans. Pattern Anal. Mach. Intell.* **1980**, *PAMI-2*, 204–222. [[CrossRef](#)]
25. Yang, P.; Yang, G. Feature Extraction Using Dual-Tree Complex Wavelet Transform and Gray Level Co-Occurrence Matrix. *Neurocomputing* **2016**, *197*, 212–220. [[CrossRef](#)]
26. Wang, S.; Xia, Y.; Liu, Q.; Luo, J.; Zhu, Y.; Feng, D.D. Gabor Feature Based Nonlocal Means Filter for Textured Image Denoising. *J. Vis. Commun. Image Represent.* **2012**, *23*, 1008–1018. [[CrossRef](#)]
27. Rafi, M.; Mukhopadhyay, S. Texture Description Using Multi-Scale Morphological GLCM. *Multimed. Tools Appl.* **2018**, *77*, 30505–30532. [[CrossRef](#)]
28. Silva, L.E.V.; Duque, J.J.; Felipe, J.C.; Murta Jr, L.O.; Humeau-Heurtier, A. Two-Dimensional Multiscale Entropy Analysis: Applications to Image Texture Evaluation. *Signal Process.* **2018**, *147*, 224–232. [[CrossRef](#)]
29. Zhang, D.-D.; Xie, F.; Zhang, L. Preprocessing and Fusion Analysis of GF-2 Satellite Remote-Sensed Spatial Data. In Proceedings of the 2018 International Conference on Information Systems and Computer Aided Education (ICISCAE), Changchun, China, 6–8 July 2018; pp. 24–29.
30. Cao, J.; Deng, Z.; Li, W.; Hu, Y. Remote Sensing Inversion and Spatial Variation of Land Surface Temperature over Mining Areas of Jixi, Heilongjiang, China. *PeerJ* **2020**, *8*, e10257. [[CrossRef](#)]
31. Zheng, Y.; Dai, Q.; Tu, Z.; Wang, L. Guided Image Filtering-Based Pan-Sharpener Method: A Case Study of GaoFen-2 Imagery. *ISPRS Int. J. Geo-Inf.* **2017**, *6*, 404. [[CrossRef](#)]
32. Jia, K.; Liu, J.; Tu, Y.; Li, Q.; Sun, Z.; Wei, X.; Yao, Y.; Zhang, X. Land Use and Land Cover Classification Using Chinese GF-2 Multispectral Data in a Region of the North China Plain. *Front. Earth Sci.* **2019**, *13*, 327–335. [[CrossRef](#)]

33. Sun, J.; Yang, J.; Zhang, C.; Yun, W.; Qu, J. Automatic Remotely Sensed Image Classification in a Grid Environment Based on the Maximum Likelihood Method. *Math. Comput. Model.* **2013**, *58*, 573–581. [[CrossRef](#)]
34. Liu, K.; Shi, W.; Zhang, H. A Fuzzy Topology-Based Maximum Likelihood Classification. *ISPRS J. Photogramm. Remote Sens.* **2011**, *66*, 103–114. [[CrossRef](#)]
35. Cracknell, M.J.; Reading, A.M. Geological Mapping Using Remote Sensing Data: A Comparison of Five Machine Learning Algorithms, Their Response to Variations in the Spatial Distribution of Training Data and the Use of Explicit Spatial Information. *Comput. Geosci.* **2014**, *63*, 22–33. [[CrossRef](#)]
36. Awad, M.; Khanna, R. Support Vector Machines for Classification. In *Efficient Learning Machines*; Apress: Berkeley, CA, USA, 2015; pp. 39–66.
37. Mountrakis, G.; Im, J.; Ogole, C. Support Vector Machines in Remote Sensing: A Review. *ISPRS J. Photogramm. Remote Sens.* **2011**, *66*, 247–259. [[CrossRef](#)]
38. Haralick, R.M.; Shanmugam, K.; Dinstein, I. Textural Features for Image Classification. *IEEE Trans. Syst. Man Cybern.* **1973**, *SMC-3*, 610–621. [[CrossRef](#)]
39. Julesz, B. Visual Pattern Discrimination. *IRE Trans. Inf. Theory* **1962**, *8*, 84–92. [[CrossRef](#)]
40. Lobos, R.; Silva, J.F.; Ortiz, J.M.; Díaz, G.; Egaña, A. Analysis and Classification of Natural Rock Textures Based on New Transform-Based Features. *Math. Geosci.* **2016**, *48*, 835–870. [[CrossRef](#)]
41. Park, Y.; Guldmann, J.-M. Measuring Continuous Landscape Patterns with Gray-Level Co-Occurrence Matrix (GLCM) Indices: An Alternative to Patch Metrics? *Ecol. Indic.* **2020**, *109*, 105802. [[CrossRef](#)]
42. Iqbal, N.; Mumtaz, R.; Shafi, U.; Zaidi, S.M.H. Gray Level Co-Occurrence Matrix (GLCM) Texture Based Crop Classification Using Low Altitude Remote Sensing Platforms. *PeerJ Comput. Sci.* **2021**, *7*, e536. [[CrossRef](#)]
43. Srivastava, D.; Rajitha, B.; Agarwal, S.; Singh, S. Pattern-Based Image Retrieval Using GLCM. *Neural Comput. Appl.* **2020**, *32*, 10819–10832. [[CrossRef](#)]
44. Lever, J.; Krzywinski, M.; Altman, N. Principal Component Analysis. *Nat. Methods* **2017**, *14*, 641–642. [[CrossRef](#)]
45. Deng, J.S.; Wang, K.; Deng, Y.H.; Qi, G.J. PCA-based Land-use Change Detection and Analysis Using Multitemporal and Multisensor Satellite Data. *Int. J. Remote Sens.* **2008**, *29*, 4823–4838. [[CrossRef](#)]
46. Pour, A.B.; Park, T.-Y.S.; Park, Y.; Hong, J.K.; Muslim, A.M.; Läufer, A.; Crispini, L.; Pradhan, B.; Zoheir, B.; Rahmani, O.; et al. Landsat-8, Advanced Spaceborne Thermal Emission and Reflection Radiometer, and WorldView-3 Multispectral Satellite Imagery for Prospecting Copper-Gold Mineralization in the Northeastern Inglefield Mobile Belt (IMB), Northwest Greenland. *Remote Sens.* **2019**, *11*, 2430. [[CrossRef](#)]
47. Amer, R.; Kusky, T.; El Mezayen, A. Remote Sensing Detection of Gold Related Alteration Zones in Um Rus Area, Central Eastern Desert of Egypt. *Adv. Space Res.* **2012**, *49*, 121–134. [[CrossRef](#)]
48. Liu, L.; Zhou, J.; Jiang, D.; Zhuang, D.; Mansaray, L.R.; Zhang, B. Targeting Mineral Resources with Remote Sensing and Field Data in the Xiemisitai Area, West Junggar, Xinjiang, China. *Remote Sens.* **2013**, *5*, 3156–3171. [[CrossRef](#)]
49. Li, C.-F.; Yin, J.-Y. Variational Bayesian Independent Component Analysis-Support Vector Machine for Remote Sensing Classification. *Comput. Electr. Eng.* **2013**, *39*, 717–726. [[CrossRef](#)]
50. Stone, J.V. Independent Component Analysis: An Introduction. *Trends Cogn. Sci.* **2002**, *6*, 59–64. [[CrossRef](#)] [[PubMed](#)]
51. Pour, A.B.; Park, T.-Y.S.; Park, Y.; Hong, J.K.; Zoheir, B.; Pradhan, B.; Ayoobi, I.; Hashim, M. Application of Multi-Sensor Satellite Data for Exploration of Zn–Pb Sulfide Mineralization in the Franklinian Basin, North Greenland. *Remote Sens.* **2018**, *10*, 1186. [[CrossRef](#)]
52. Gholami, R.; Moradzadeh, A.; Yousefi, M. Assessing the Performance of Independent Component Analysis in Remote Sensing Data Processing. *J. Indian Soc. Remote Sens.* **2012**, *40*, 577–588. [[CrossRef](#)]
53. Liu, L.; Li, C.; Lei, Y.; Yin, J.; Zhao, J. Feature Extraction for Hyperspectral Remote Sensing Image Using Weighted PCA-ICA. *Arab. J. Geosci.* **2017**, *10*, 307. [[CrossRef](#)]
54. Pour, A.B.; Park, Y.; Crispini, L.; Läufer, A.; Kuk Hong, J.; Park, T.-Y.S.; Zoheir, B.; Pradhan, B.; Muslim, A.M.; Hossain, M.S.; et al. Mapping Listvenite Occurrences in the Damage Zones of Northern Victoria Land, Antarctica Using ASTER Satellite Remote Sensing Data. *Remote Sens.* **2019**, *11*, 1408. [[CrossRef](#)]
55. Altman, N.; Krzywinski, M. The Curse(s) of Dimensionality. *Nat. Methods* **2018**, *15*, 399–400. [[CrossRef](#)] [[PubMed](#)]
56. Kavzoglu, T.; Tonbul, H.; Yildiz Erdemir, M.; Colkesen, I. Dimensionality Reduction and Classification of Hyperspectral Images Using Object-Based Image Analysis. *J. Indian Soc. Remote Sens.* **2018**, *46*, 1297–1306. [[CrossRef](#)]
57. Baid, S.; Tabit, A.; Algouti, A.; Algouti, A.; Nafouri, I.; Souddi, S.; Aboulfaraj, A.; Ezzahzi, S.; Elghouat, A. Lithological Discrimination and Mineralogical Mapping Using Landsat-8 OLI and ASTER Remote Sensing Data: Igoudrane Region, Jbel Saghro, Anti Atlas, Morocco. *Heliyon* **2023**, *9*, e17363. [[CrossRef](#)] [[PubMed](#)]
58. Pereira, J.; Pereira, A.J.S.C.; Gil, A.; Mantas, V.M. Lithology Mapping with Satellite Images, Fieldwork-Based Spectral Data, and Machine Learning Algorithms: The Case Study of Beiras Group (Central Portugal). *Catena* **2023**, *220*, 106653. [[CrossRef](#)]
59. Goodarzi Mehr, S.; Ahadnejad, V.; Abbaspour, R.A.; Hamzeh, M. Using the Mixture-Tuned Matched Filtering Method for Lithological Mapping with Landsat TM5 Images. *Int. J. Remote Sens.* **2013**, *34*, 8803–8816. [[CrossRef](#)]
60. Xi, Y.; Mohamed Taha, A.M.; Hu, A.; Liu, X. Accuracy Comparison of Various Remote Sensing Data in Lithological Classification Based on Random Forest Algorithm. *Geocarto Int.* **2022**, *37*, 14451–14479. [[CrossRef](#)]

61. Lin, J.; Wang, R.; Zhao, B.; Cheng, S. A Comprehensive Scheme for Lithological Mapping Using Sentinel-2A and ASTER GDEM in Weathered and Vegetated Coastal Zone, Southern China. *Open Geosci.* **2019**, *11*, 982–996. [[CrossRef](#)]
62. Kumar, C.; Chatterjee, S.; Oommen, T.; Guha, A.; Mukherjee, A. Multi-Sensor Datasets-Based Optimal Integration of Spectral, Textural, and Morphological Characteristics of Rocks for Lithological Classification Using Machine Learning Models. *Geocarto Int.* **2022**, *37*, 6004–6032. [[CrossRef](#)]
63. Mars, J.C. Mineral and Lithologic Mapping Capability of Worldview 3 Data at Mountain Pass, California, Using True- and False-Color Composite Images, Band Ratios, and Logical Operator Algorithms. *Econ. Geol.* **2018**, *113*, 1587–1601. [[CrossRef](#)]
64. Shebl, A.; Csámer, Á. Stacked Vector Multi-Source Lithologic Classification Utilizing Machine Learning Algorithms: Data Potentiality and Dimensionality Monitoring. *Remote Sens. Appl. Soc. Environ.* **2021**, *24*, 100643. [[CrossRef](#)]
65. Ninomiya, Y.; Fu, B. Regional Lithological Mapping Using ASTER-TIR Data: Case Study for the Tibetan Plateau and the Surrounding Area. *Geosci. Switz.* **2016**, *6*, 39. [[CrossRef](#)]
66. Wang, Z.; Zuo, R.; Dong, Y. Mapping Himalayan Leucogranites Using a Hybrid Method of Metric Learning and Support Vector Machine. *Comput. Geosci.* **2020**, *138*, 104455. [[CrossRef](#)]

Disclaimer/Publisher’s Note: The statements, opinions and data contained in all publications are solely those of the individual author(s) and contributor(s) and not of MDPI and/or the editor(s). MDPI and/or the editor(s) disclaim responsibility for any injury to people or property resulting from any ideas, methods, instructions or products referred to in the content.